RNA Selectively Modulates Activity of Virulent Amyloid PSMα3 and Host Defense LL-37 via Phase Separation and Aggregation Dynamics

Bader Rayan[1], Eilon Barnea[1], Rinat Indig[1], Christian F. Pantoja[2], Jesse Gayk[3], Yael Lupu-Haber[4], Alexander Upcher[5], Amir Argoetti[1], Jacob Aunstrup Larsen[6], Alexander K. Buell[6], Markus Zweckstetter[2,7], and Meytal Landau[1,3,8,9*]

[1] Department of Biology, Technion-Israel Institute of Technology, Haifa 3200003, Israel

[2] German Center for Neurodegenerative Diseases (DZNE), 37075 Göttingen, Germany

[3] CSSB Centre for Structural Systems Biology, Deutsches Elektronen-Synchrotron DESY, 22607 Hamburg, Germany

[4] The Life Sciences and Engineering Infrastructure Center, Technion-Israel Institute of Technology, Haifa 3200003, Israel

[5] Ilse Katz Institute for Nanoscale Science and Technology, Ben Gurion University of the Negev, Beer-Sheva, Israel

[6] Department of Biotechnology and Biomedicine, Technical University of Denmark DTU, 2800 Kongens Lyngby, Denmark

[7] Department for NMR-based Structural Biology, Max Planck Institute for Multidisciplinary Sciences, 37077 Göttingen, Germany

[8] The Center for Experimental Medicine, Universitätsklinikum Hamburg-Eppendorf (UKE), Hamburg, Germany

[9] European Molecular Biology Laboratory (EMBL), Hamburg, Germany

* Correspondence to meytal.landau@desy.de

Abstract

Amyloids, classically associated with neurodegenerative disease, also play important roles in infection and immunity. Phenol-soluble modulins (PSMs) from *Staphylococcus aureus* are amyloid-forming virulence peptides that contribute to cytotoxicity, immune modulation, and biofilm stability. PSMα3 forms cross-α amyloid fibrils and shares sequence and α-helical self-assembly features with LL-37, a human host-defence peptide that forms non-amyloid α-helical assemblies. Here, we identify RNA as a context-dependent regulator of their assembly pathways and biological activity. RNA consistently reduces LL-37 cytotoxicity toward human cells without compromising its antibacterial function, suggesting a host-protective effect. In contrast, RNA preserves PSMα3 cytotoxic and antimicrobial activity over time by reshaping its assembly landscape, promoting liquid–liquid phase separation at low concentrations and stabilizing dynamic α-helical intermediates. At higher RNA concentrations, both peptides transition into distinct aggregated states, amorphous for LL-37 and fibrillar for PSMα3, correlating with divergent functional outcomes. The amyloid inhibitor EGCG abolishes the bioactivity of both peptides by redirecting assembly into non-functional aggregates, highlighting that activity depends on supramolecular architecture and reversibility rather than aggregation per se. Together, these findings establish RNA as an environmental regulator of α-helical peptide assemblies and reveal phase transitions as tuneable determinants of peptide function, with implications for microbial virulence, innate immunity, and therapeutic intervention in infectious and protein-aggregation–associated diseases.

Introduction

Bacterial amyloids are proteins capable of forming ordered fibrils, playing a crucial role in biofilm stability, surface adherence, cell toxicity and immune responses[1–6]. These amyloids are vital for the survival and virulence of many bacteria, enabling them to colonize and persist in diverse environments[7,8]. Some examples of bacterial amyloids include the Csg and Fap proteins from *Enterobacteria* and *Pseudomonas* species[1,6,7,9–11], respectively, which play a role in biofilm stability. Staphylococcal phenol-soluble modulins (PSMs) are short peptides that are capable of forming amyloid structures[12–20] and perform multiple roles central to pathogenesis and immune evasion in *Staphylococcus aureus*[21–36] . In this context, defining PSMs as "functional amyloids" implies that amyloid formation can serve regulatory purposes, including controlled storage, stabilization, or spatial organization of bioactive molecules, as described for peptide hormones[37] and RNA-binding proteins[38,39]. Accordingly, amyloid assembly may function as a reversible structural state that modulates the availability and timing of virulence-associated activities.

Among bacterial amyloids, PSMα3 is notable for its strong cytotoxicity toward a broad range of microbial and human cell types[28,34,40–42] and for adopting a unique cross-α amyloid architecture, in which α-helices stack perpendicular to the fibril axis in paired sheets[14–16]. Recent studies on fibril-forming antimicrobial peptides have suggested a correlation between α-helical conformations in the solid state and cytotoxicity[43–47]. This observation parallels findings in human disease-associated amyloids, where α-helical oligomeric intermediates are widely considered to represent the toxic species[48–50]. Similarly, within the PSMα family, distinct amyloid polymorphs appear to encode different biological functions[31]: the metastable and reversible cross-α assemblies of PSMα3 enable dynamic switching between inactive and active states, whereas the more stable and irreversible cross-β fibrils formed by the homologous PSMα1 peptide[19,51] may contribute to robust biofilm architecture. In this framework, toxicity is proposed to arise from transient assembly intermediates along the fibrillation pathway rather than from the mature fibrils themselves[52].

PSMα3 shares self-assembly of α-helices with LL-37, a human host defence peptide[53–55], even though LL-37 is not an amyloid and does not form canonical cross-α or cross-β fibrils. Moreover, the LL-37 antimicrobial active core (residues 17–29) shows sequence similarity to PSMα3, and the formation of non-amyloid fibrils composed of densely packed cationic amphipathic α-helices[56]. The sequence and α-helices self-assembly similarities supported the hypothesis that PSMα3 might recapitulate functions of LL-37, and indeed, they share the activation of the signal inhibitory receptor on leukocytes-1 (SIRL-1) which is a negative regulator of myeloid cell function and dampens antimicrobial responses[57]. Such common functions might be related to molecular mimicry and the ability of bacterial peptides to hijack immunomodulation pathways[58]. Indeed, PSMαs interact with the formyl peptide receptor 2 (FPR2) on immune cells, initiating immune responses such as chemotaxis, phagocytosis, and the secretion of pro-inflammatory cytokines. These reactions are critical for recruiting and activating immune cells, thereby amplifying the inflammatory response[23,59–64].

LL-37 has been shown to bind RNA released from dying cells, forming stable complexes that protect the RNA from enzymatic degradation and promote its uptake by dendritic cells[65]. Once internalized, these RNA–LL-37 complexes activate Toll-like receptors (TLRs), triggering cytokine production and dendritic cell maturation[65,66]. Beyond LL-37, other human AMPs, such as β-defensins, also form higher-order assemblies that organize nucleic acids into nanostructures with defined periodicity. These nanocomplexes potently stimulate TLRs, highlighting that innate immune activation is influenced not only by ligand identity, but also by the nanoscale geometry and spatial organization of the complexes[67–69].

Interestingly, nucleic acid interactions also play a key role in the immune activation triggered by bacterial amyloids. For example, PSMs co-assemble with extracellular DNA (eDNA), and CpG-rich DNA specifically promotes PSMα3 fibrillation, forming co-aggregates that colocalize with DNA in biofilms. These complexes activate TLR pathways and induce anti-dsDNA autoantibody responses in mice[27]. Similar mechanisms are seen in *E. coli* and *Salmonella*, where curli fibers bind eDNA, enhance fibrillation, and engage TLRs signaling, also promoting

autoimmunity[70,71]. These findings suggest that amyloid–DNA complexes in bacterial biofilms are not only structural components but also potent immunomodulators with potential links to autoimmunity.

Given their shared cationic, amphipathic α-helical character, but distinct amyloidogenic properties, we sought to examine whether RNA differentially influences the assembly landscapes and bioactivity of PSMα3 and LL-37. RNA is increasingly recognized as a key regulator of protein phase behaviour, capable of promoting liquid–liquid phase separation (LLPS), altering aggregation pathways, and reshaping supramolecular organization. LLPS is a fundamental mechanism of cellular organization, in which biomolecules demix into dynamic, membraneless compartments that regulate processes such as RNA metabolism, stress responses, and signal transduction[72–75]. Whether bacterial virulence-associated peptides are similarly governed by RNA-mediated phase behaviour remains largely unexplored.

To address this, we investigated how defined RNA species modulate the structural transitions, material properties, and bioactivity of PSMα3 and LL-37. In parallel, we examined the impact of epigallocatechin gallate (EGCG), a small-molecule assembly modulator widely studied as an amyloid inhibitor[32,76–78], to compare RNA-driven regulation with pharmacological redirection of peptide assembly. By integrating biophysical, structural, and cellular approaches, this work aims to define how environmental factors reshape α-helical peptide assemblies and thereby influence bacterial virulence and host-defence mechanisms.

Results

PSMα3 interacts with RNA in vitro

The interactions between PSMα3 and RNA were assessed using an Electrophoretic Mobility Shift Assay (EMSA), comparing the binding affinity of PSMα3 to single-stranded PolyA RNA and double-stranded Poly (AU) RNA. These RNAs were selected as simplified, well-defined model RNAs to probe general peptide–RNA interactions in an unbiased manner, as no prior

information was available regarding whether such interactions occur, or which specific RNA species might be involved. The RNA molecules were labelled with the IR800CW fluorescent dye (as detailed in the Methods section). Freshly dissolved PSMα3, at varying concentrations, was incubated with each RNA type at a constant concentration for 30 minutes at 37°C. The EMSA results revealed that PSMα3 exhibits a stronger binding affinity to double-stranded Poly (AU) RNA, as evidenced by significant shifts at lower peptide concentrations compared to single-stranded Poly (A) (Fig. 1).

Quantification of free and shifted RNA band intensities revealed a progressive increase in the fraction of RNA bound as a function of peptide concentration for both RNA molecules (Fig. S1). Poly (AU) RNA reached saturation at lower PSMα3 concentrations than Poly (A), consistent with stronger apparent binding. Fitting the binding curves to a Hill model yielded an apparent dissociation constant (Kd) of 61.8 ± 1.6 μM for Poly (AU) and 94.5 ± 5.4 μM for Poly (A) (Fig. S1). Hill coefficients greater than 1 were obtained for both RNAs, consistent with cooperative binding behaviour. Based on these Kd differences, subsequent experiments focused on PSMα3 behaviour in the presence of double-stranded Poly (AU) RNA (hereafter referred to as RNA).

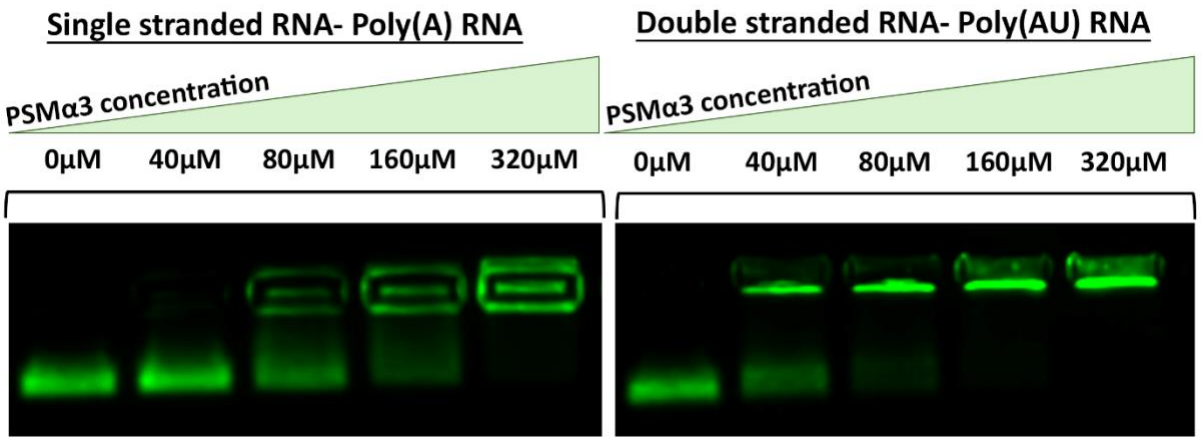

Figure 1. The binding and effect of single- and double-stranded RNA on PSMα3. EMSA assay illustrating the interaction between PSMα3 and RNA. The assay compares the effects of increasing concentrations of PSMα3 (0 μM, 40 μM, 80 μM, 160 μM, and 320 μM), shown in a gradient from left to right, on the mobility shift of single-stranded Poly (A) RNA (left panel) and double-stranded Poly (AU) RNA (right panel) at ~400ng/μL.

Non-monotonic turbidity response of PSMα3 to RNA

In order to assess the concentration-dependent effect of RNA on PSMα3 we used turbidity assays. The results showed that a 30 min co-incubation of 100 μM PSMα3 with varying concentrations of RNA displayed an increased turbidity up to 50 ng/μl, while higher RNA concentrations displayed a decrease in turbidity (Fig. S2). The decrease in particle size above 50 ng/μL can be a result of either the formation of smaller particles or aggregation into larger clusters, which can settle out of suspension, removing them from the light-scattering medium and reducing turbidity. Alternatively, this non-monotonic turbidity behaviour is conceptually similar to charge-driven re-entrant transitions described in other protein–RNA phase-separating systems, such as Ddx4[79], however, the molecular context and assembly architecture of PSMα3 are fundamentally distinct. According to the turbidity results, we hypothesized that 50 ng/μl can be a critical concentration between soluble species, which might be able to phase separate, and the formation of aggregates.

RNA concentration regulates formation and liquid-to-solid transition of PSMα3 condensates

To better understand the nature of the PSMα3-RNA interaction, we visualized their mixtures via fluorescence microscopy, using PSMα3 labelled with Fluorescein isothiocyanate (FITC) at the C-terminus (PSMα3-FITC), which is known to form fibrils[14]. All fluorescence microscopy experiments used a mixture of 20% FITC-labelled and 80% unlabelled peptide to minimize potential effects of the fluorophore on assembly behaviour. 100 μM PSMα3-FITC was incubated with either 50 ng/μl or 400 ng/μl RNA, labelled using propidium iodide (PI), in a close to physiological buffer of 50 mM HEPES (pH 7.4) containing 150 mM sodium chloride (NaCl).

Upon addition of 50 ng/μL RNA, PSMα3 formed liquid–liquid phase-separated droplets that clearly colocalized with RNA (Fig. 2A). We further observed encapsulation of RNA within PSMα3–FITC–coated condensates (Fig. S3), indicating co-assembly rather than simple surface association. The liquid-like nature of these droplets was confirmed by fluorescence

recovery after photobleaching (FRAP), which showed rapid signal recovery shortly after bleaching (Fig. 2B). Quantitative analysis revealed a half-time of recovery of 3.1 seconds and a mobile fraction of 68% (immobile fraction 32%) (Fig. S4), consistent with dynamic molecular exchange. Across multiple samples, we consistently observed coexistence of small droplets and larger aggregates. The experimental timescales examined do not allow us to reliably determine whether diffusion-driven coalescence kinetics would support classical droplet ripening dynamics[80,81]. Notably, after 2 hours of incubation, fluorescence recovery was no longer detected (Fig. 2C), indicating that the condensates undergo time-dependent aging and transition toward a more solid-like or aggregated state.

In contrast to the effect of 50 ng/µl RNA, the addition of a higher RNA concentration of 400 ng/µl to PSMα3 resulted in immediate aggregation, with no observed phase of droplet formation (Fig. 2D). FRAP analysis indicated no recovery of signal after bleaching, likely due to the formation of solid structures rather than droplets with liquid-like properties (Fig. 2E). In the absence of RNA, PSMα3 did not form condensates and instead appeared as dispersed or irregular assemblies (Fig. 2F), establishing that RNA is required to induce the droplet state observed under these conditions.

Colocalization between PSMα3-FITC and RNA was quantified using Pearson's correlation coefficient (above the Costes threshold) and Manders' overlap coefficients (tM1 and tM2) (Fig. S5). All metrics indicate substantially stronger spatial correlation and signal overlap at 50 ng/µL RNA compared with 400 ng/µL RNA. At low RNA concentration, Pearson's correlation is positive ($R \approx 0.53$), accompanied by high Manders' overlap values ($tM1 \approx 0.68$; $tM2 \approx 0.63$). This is consistent with coordinated association of PSMα3 and RNA within liquid-like droplets. In contrast, at 400 ng/µL RNA, Pearson's correlation becomes negative ($R \approx -0.24$) and Manders' coefficients are markedly reduced. This indicates a transition from co-localized droplet assemblies to spatially segregated aggregated structures in which RNA becomes partially excluded from the peptide-rich structures.

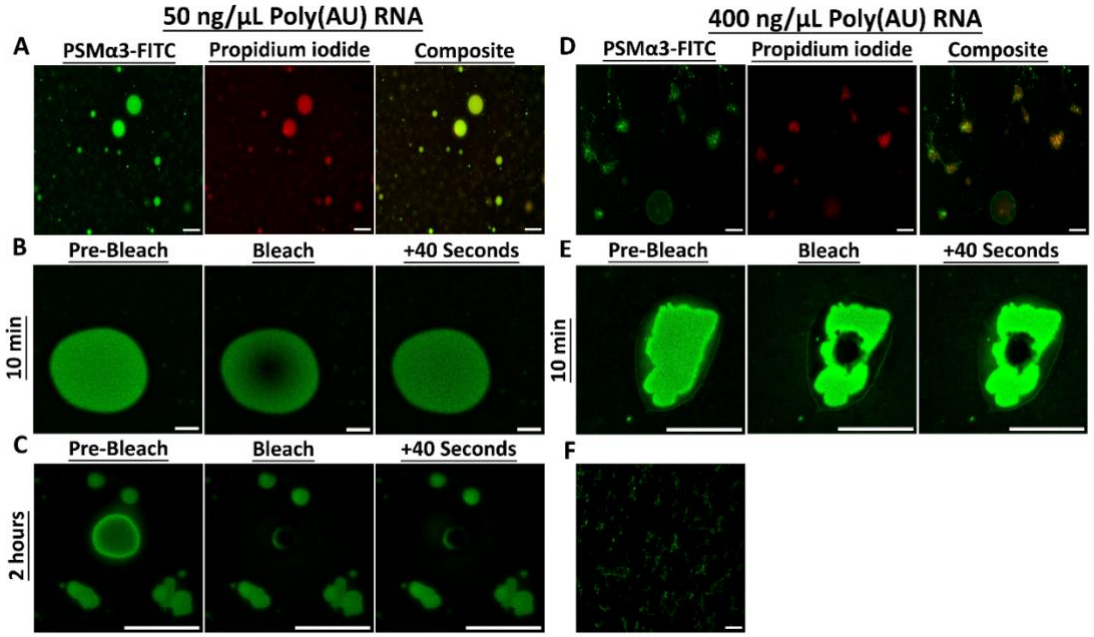

Figure 2. Colocalization, droplet formation, and texture of PSMα3 mixed with varying Poly (AU) RNA concentrations. Widefield fluorescence microscopy images of 100 µM of 20% FITC-PSMα3 (green) and 80% unlabelled PSMα3 incubated with Poly (AU) RNA (red) at 50 ng/µL (**A**) or 400 ng/µL (**D**), shown as individual fluorescence channels and merged images. (**B-C**) FRAP analysis of PSMα3-FITC in the presence of 50 ng/µL Poly (AU) RNA after 10 min (**B**) or 2 h (**C**) of co-incubation. (**E**) FRAP analysis of PSMα3-FITC in the presence of 400 ng/µL Poly (AU) RNA after 10 min of co-incubation. For panels B, C, and E, images were acquired before photobleaching, immediately after photobleaching, and 40 s post-photobleaching. (**F**) 100 µM of 20% FITC-PSMα3 (green) and 80% unlabelled PSMα3 in the absence of RNA. All scale bars represent 20 µm.

RNA concentration-driven changes in PSMα3 fibrillar morphology and aggregation

The TEM micrographs showed that in the absence of RNA, 100 µM PSMα3 formed nanotube-like fibrils after 2 hours, growing wider or with some twist after 24-hours co-incubation (Fig. 3A). Incubating PSMα3 with a low concentration of 10 ng/µL RNA displayed accelerated fibril formation, with more strongly twisted, wide, sheet-like fibrils observed after both 2 hours and 24 hours (Fig. 3A). With the addition of 50 ng/µL RNA, PSMα3 fibrils have a similar twisted morphology after 2 hours, while at a longer incubation time of 24 hours, we observed a

significant morphological shift into more thin amorphous aggregates (Fig. 3A). At the higher concentration of 400 ng/μL RNA, PSMα3 formed dense, thin fibrils after 2 hours, but with a possible fragmentation into smaller species or rearrangement into amorphous aggregates after 24 hours of co-incubation. This indicates that RNA concentration and time of co-incubation affect the density and morphology of PSMα3 fibrils. This corresponds to the differences observed by light microscopy of co-aggregates contexture of LLPS droplets vs solid aggregates (Fig. 2).

These observations were further supported by TIRF microscopy using the amyloid-specific dye AmyTracker630 (AT630). With the addition of 50 ng/μL RNA to PSMα3-FITC, a strong AT630 fluorescence signal was detected only after 2 hours of co-incubation, but not after 30 minutes (Fig. 3B, quantified in Fig. S6). This suggests a time-dependent transition into amyloid-like species. Conversely, at 400 ng/μL RNA, a significant AT630 fluorescence was observed already after 30 minutes of co-incubation, consistent with a rapid formation of amyloid fibrils (Figs. 3C and S6). These findings highlight a concentration- and time-dependent modulation of PSMα3 phase separation and structural transitions, where RNA promotes LLPS at lower concentrations and drives rapid amyloid formation and unique fibrillar morphologies at higher concentrations. Future work will be required to quantitatively define the phase boundaries and delineate the dominant mechanisms, such as sedimentation, dissolution, or coarsening/aging, across intermediate RNA concentrations.

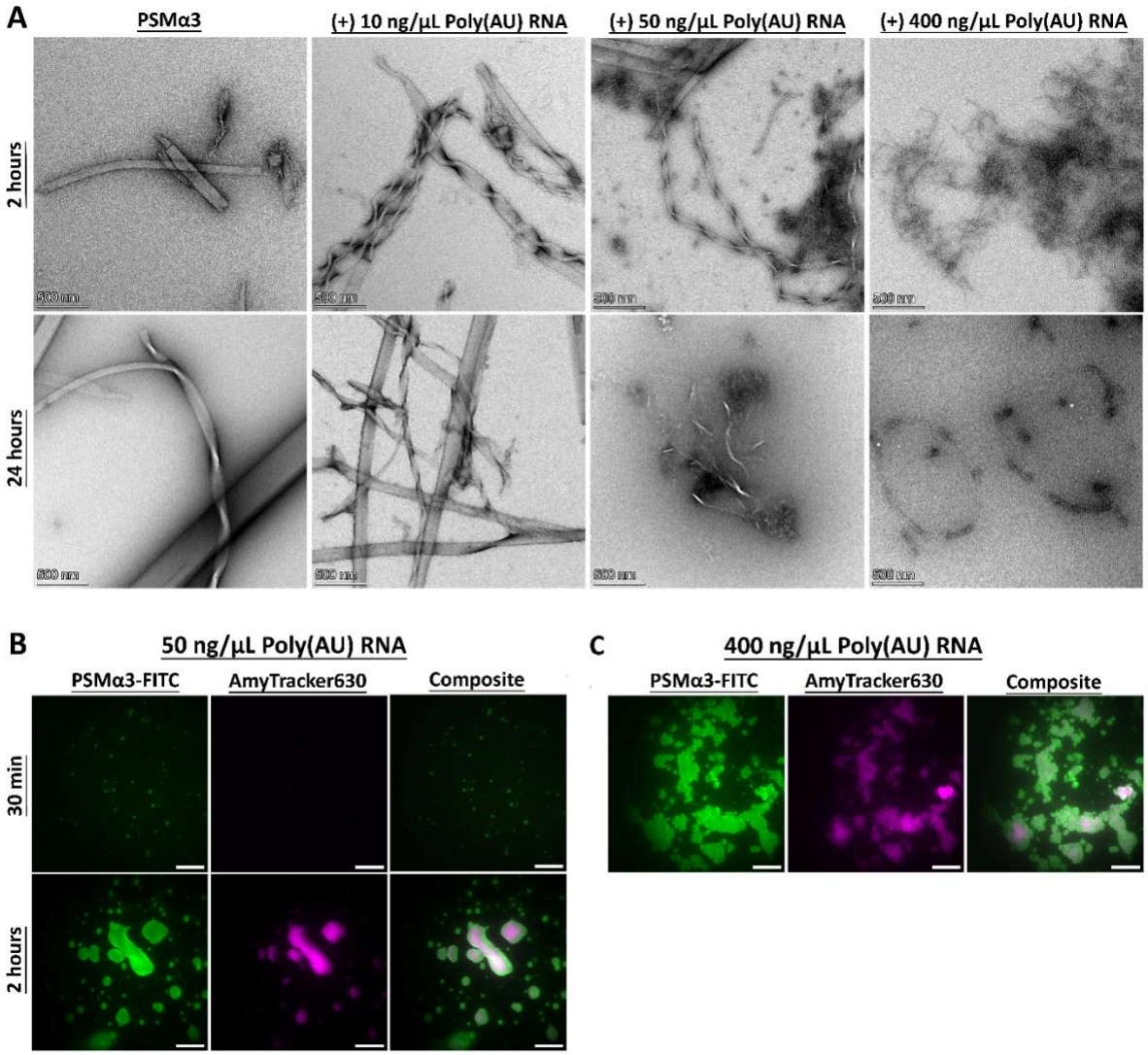

Figure 3. TEM and TIRF visualization of PSMα3 aggregation and morphology with different Poly (AU) RNA concentrations and incubation times. (A) TEM micrographs of 100 µM PSMα3 incubated with or without Poly (AU) RNA at varying concentrations of 10 ng/µL, 50 ng/µL, and 400 ng/µL for 2 hours (top row) and 24 hours (bottom row). Scale bars represent 500 nm. **(B)** TIRF microscopy images showing 100 µM of 20% FITC-PSMα3 (green) and 80% unlabelled PSMα3 co-incubated with 50 ng/µL Poly (AU) RNA and the amyloid indicator AT630 (magenta) for 30 minutes and 2 hours. Scale bars represent 20 µm. **(C)** TIRF microscopy images of 100 µM of 20% FITC-PSMα3 (green) and 80% unlabelled PSMα3 co-incubated with 400 ng/µL Poly (AU) RNA and AT630 (magenta) for 30 min. Scale bars represent 20 µm.

RNA enhances α-helical structure of PSMα3

Solid-state circular dichroism (ssCD) spectroscopy reveals that PSMα3 lacks a defined secondary structure both immediately after preparation and following 2 hours of incubation (Fig. S7). However, an α-helical signature of PSMα3 is markedly enhanced in the presence of RNA compared to peptide alone, as evidenced by increased signal intensity, deeper minima, and more pronounced spectral features characteristic of α-helical structure. This enhancement is more pronounced at 400 ng/μL RNA than at 50 ng/μL, particularly after 2 hours of co-incubation, indicating that RNA concentration influences the stabilization of α-helical assemblies. This supports the notion that RNA not only accelerates aggregation but also promotes or stabilizes the α-helical fibrillar architecture, potentially consistent with cross-α amyloid structures.

RNA modulates the antibacterial activity of PSMα3

The antimicrobial activity of PSMα3 against *Escherichia coli* was evaluated under varying RNA concentrations and incubation times using the PrestoBlue Cell Viability Assay (Fig. 4A). Freshly dissolved 10 or 20 μM PSMα3 exhibited potent antibacterial activity, completely abolishing bacterial viability. After 2 hours of incubation, PSMα3 retained its full activity, comparable to its freshly prepared state. The presence of RNA at 50 ng/μL and 400 ng/μL had no impact on its antimicrobial function within this timeframe (Fig. 4A).

In contrast, after 24 hours of incubation, PSMα3's antibacterial activity was significantly reduced (Fig. 4A), suggesting a decrease in its effective concentration or changes in its morphology. Notably, the addition of RNA at 50 ng/μL or 400 ng/μL prevented this loss of activity, indicating that RNA plays a stabilizing role in toxic species or their reservoir. These findings suggest that RNA influences PSMα3 aggregation dynamics and morphology, thereby modulating its long-term antimicrobial effectiveness.

RNA modulates PSMα3 cytotoxicity against human HeLa cells

The effect of RNA on the cytotoxicity of PSMα3 against human HeLa cells was evaluated by measuring lactate dehydrogenase (LDH) release, an indicator of cell membrane damage (Fig. 4B). Freshly dissolved PSMα3 exhibited substantial cytotoxicity, causing approximately 80% cell death at 20 μM and 50% at 10 μM. The presence of RNA did not significantly alter the toxicity of freshly dissolved PSMα3 (Fig. 4B), similar to the antibacterial activity. However, following 2 hours of incubation, PSMα3 cytotoxicity was significantly reduced, possibly due to aggregation and a loss of active peptide concentration. This reduction occurred earlier than the loss of antibacterial activity, which was only observed after 24 hours of incubation (Fig. 4A).

Notably, co-incubation with RNA helped maintain PSMα3 cytotoxicity in a concentration-dependent manner. With 50 ng/μL RNA, the 2-hour incubated PSMα3 retained cytotoxicity comparable to its freshly dissolved form, suggesting that RNA prevents activity loss due to incubation. However, after 24 hours, 50 ng/μL RNA was insufficient to preserve cytotoxicity. In contrast, at 400 ng/μL RNA, partial cytotoxicity was maintained for both 2-hour and 24-hour incubated PSMα3, compared to the freshly dissolved sample.

Overall, these findings suggest that RNA prevents the incubation-induced loss of both antibacterial activity and cytotoxicity (Fig. 4). This effect appears to be concentration- and co-incubation time-dependent, likely linked to RNA-induced morphological variations of PSMα3 species (Figs. 2-3).

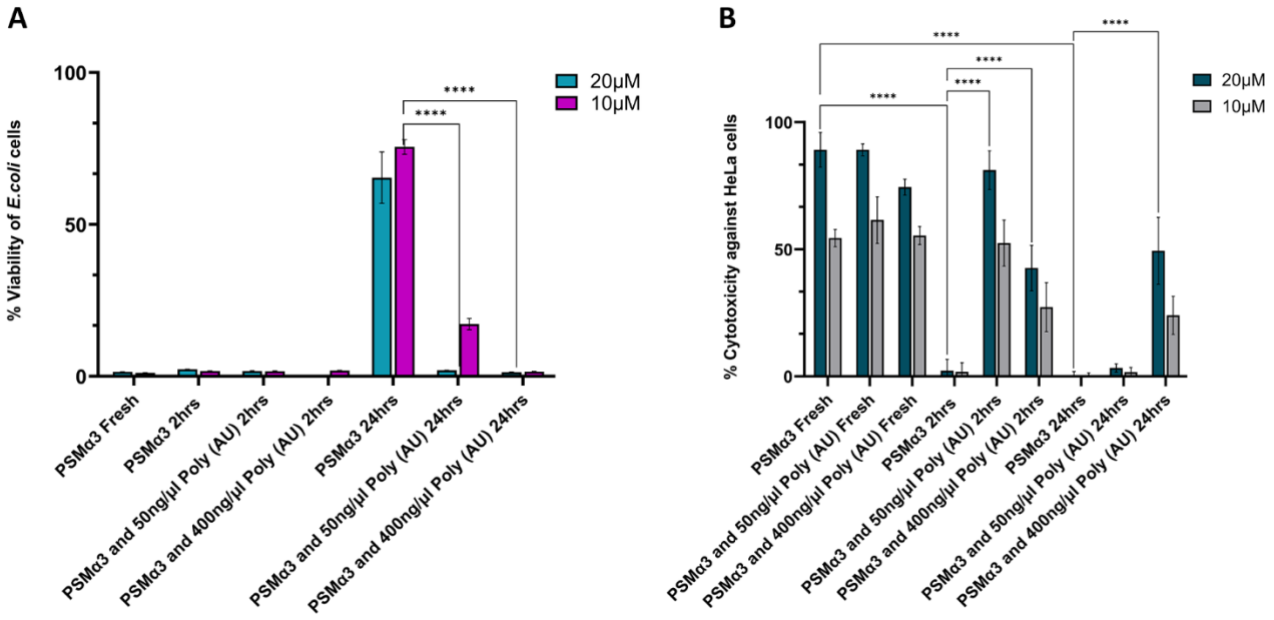

Figure 4. Impact of Poly (AU) RNA on PSMα3 cytotoxicity and antibacterial activity. Antimicrobial activity of PSMα3 against *E. Coli* using the PrestoBlue cell viability assay (**A**) and its cytotoxicity against HeLa cells using the LDH colorimetric assay (**B**) were assessed with and without Poly (AU) RNA at varying concentrations. The experiments were performed in at least three replicates and repeated across three independent days to ensure result reliability. Cytotoxicity and bacterial cell viability percentages were calculated as the mean of all replicates, with error bars representing the standard error of the mean (SEM). Statistical significance was determined using one-way ANOVA for normally distributed data in GraphPad Prism (version 11). Significance levels are indicated as follows: *p<0.05, **p<0.01, ***p<0.001, ****p<0.0001.

PSMα3 targets nucleolar nucleic acids in HeLa cells with LLPS dynamics

The interactions and localization of PSMα3 were next explored in HeLa cells with the addition of 20μM PSMα3 just before imaging. PI was added to the cell medium as a marker for cell death, as it selectively penetrates dead cells and binds to their nucleic acids.

Confocal microscopy images revealed that PSMα3 induces significant toxicity as indicated by membrane damage and blebbing, intracellular PSMα3 aggregate formation, and positive PI staining (Fig. 5 and Movie. S1). PSMα3 also enters the nuclei, with a notable concentration in

the nucleolus, indicated by the foci of green fluorescence (marked by white arrows in Fig. 5). The composite images demonstrated clear colocalization of PSMα3 with nucleic acids in the nucleolus, as seen by the overlap of the green PSMα3-FITC signal and the red fluorescence from PI-stained nucleic acids.

FRAP analysis of 20 μM PSMα3 within the nucleolus of HeLa cells revealed measurable but constrained mobility (Fig. 5B). Following photobleaching of a defined nucleolar region (indicated by the white arrow), fluorescence gradually recovered over the 60 s acquisition window, indicating dynamic exchange of PSMα3 within this compartment. However, recovery was slow and incomplete during this time frame, and did not reach a clear plateau, precluding reliable determination of recovery half-time or precise mobile and immobile fractions (Fig. S8), and indicating dynamic but constrained exchange within this RNA-rich compartment. This behaviour differs from the rapid and near-complete recovery observed for PSMα3–RNA droplets formed in vitro (Fig. 2C), indicating that nucleolar-associated PSMα3 exhibits more restricted dynamics than liquid-like condensates in defined buffer systems.

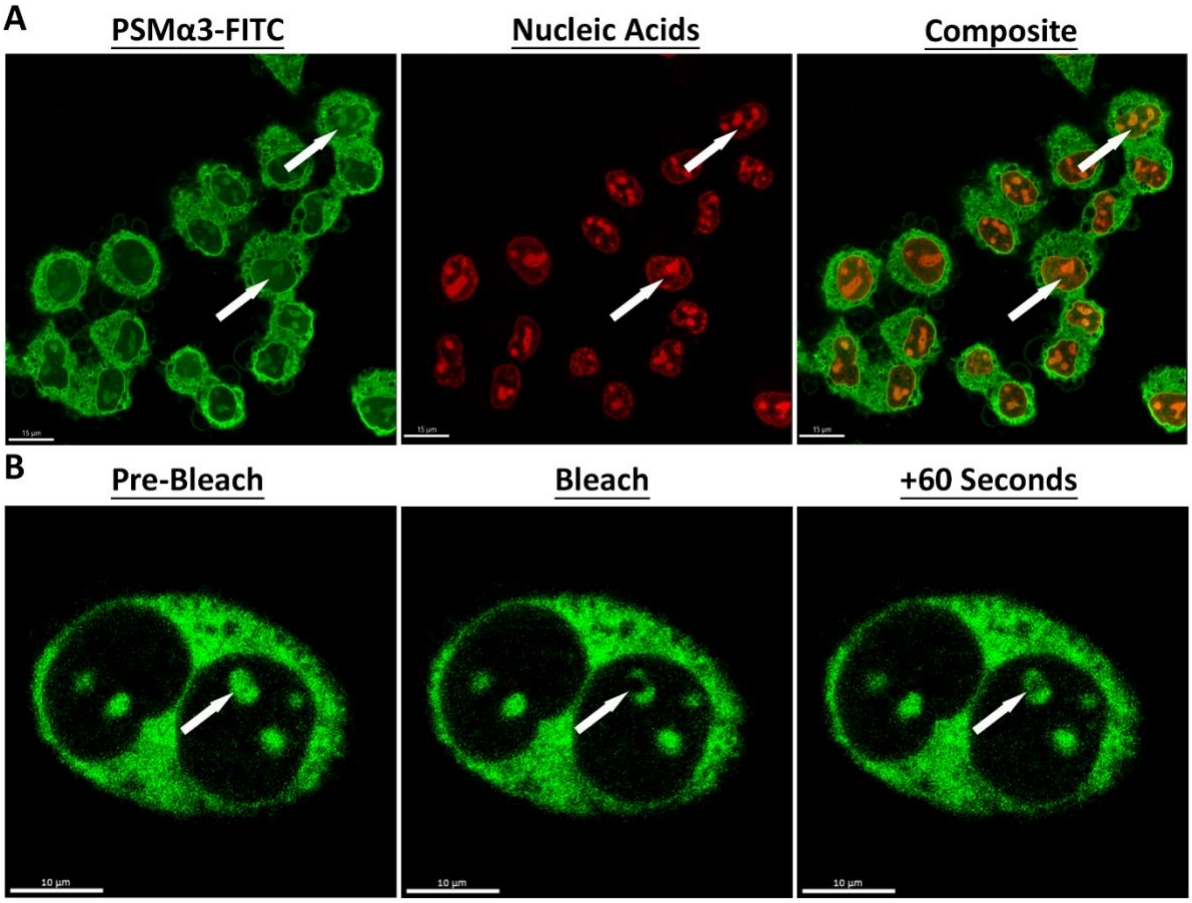

Figure 5. Colocalization of PSMα3 with nucleic acids in HeLa cells. (A) Confocal microscopy images showing the localization and colocalization of 20 μM of 20% FITC-PSMα3 (green) and 80% unlabelled PSMα3 and nucleic acids stained with PI (red) inside the nucleolus of HeLa cells (indicated in arrows). The left panel illustrates the distribution of PSMα3 within the cell. The middle panel shows the nucleic acids stained with PI. The right panel is a composite image that demonstrates the colocalization of PSMα3 with nucleic acids. Scale bars represent 15 μm. **(B)** FRAP analysis of 20 μM of 20% FITC-PSMα3 (green) and 80% unlabelled PSMα3 inside the nucleolus (indicated by the arrow) of HeLa cells, showing fluorescence recovery after 60 seconds. Scale bars represent 10 μm.

EGCG directly binds PSMα3 and inhibits its fibrillation and bioactivity, even in the presence of RNA

Since RNA appears to protect or maintain PSMα3's toxic functions, potentially by influencing its fibril formation and morphology, we investigated the corresponding and combined effects

of an inhibitor of fibril formation. One such inhibitor is epigallocatechin gallate (EGCG), the most abundant catechin in tea and a known amyloid inhibitor, including PSMs[32].

The addition of EGCG to PSMα3 at a 1:1 molar ratio did not significantly alter its cytotoxicity against HeLa cells. However, at a fivefold molar excess, EGCG completely abolished PSMα3's cytotoxic effect (Fig. 6A). To examine the structural changes underlying this effect, we analysed fibril formation kinetics and morphology in the presence of EGCG. TEM micrographs revealed that a fivefold molar excess of EGCG disrupted fibril formation of 100 μM PSMα3, instead inducing amorphous aggregates (Fig. 6B). Consistently, kinetics assays of fibril formation showed that EGCG inhibited the ThT fluorescence curve otherwise indicating the fibril formation of 100 μM PSMα3 (Fig. S9). These findings suggest that EGCG reduces PSMα3 toxicity by modulating its fibril formation and morphology. The addition of RNA did not counteract the effect of EGCG or restore PSMα3 cytotoxicity (Fig. 6A), highlighting the strong impact of EGCG on PSMα3 morphology and properties.

Live-cell confocal microscopy provided further insights into how EGCG binding affects PSMα3 interactions with cells. In accordance with the LDH measurements (Fig. 6A), in the absence of EGCG, 20 μM PSMα3 readily penetrated cells and induced robust PI staining, indicating membrane disruption (Fig. 6C, top panel and Movie. S1). In contrast, a fivefold molar excess of EGCG prevented the toxic effects of 20 μM PSMα3, blocking cell penetration and PI staining (Fig. 6C, bottom panel and Movie. S2). Instead, PSMα3-FITC formed extracellular aggregates and showed no interaction with cell membranes, as indicated by the absence of PI staining and intact cell membranes.

Furthermore, EGCG at a fivefold molar excess also reduced the antibacterial activity of PSMα3 against *E. coli*, maintaining bacterial cell viability (Fig. S10). Super-resolution fluorescence microscopy showed that while 20 μM PSMα3 typically aggregates on the bacterial membrane, causing membrane disruption and PI staining indicative of cell death (Fig. S10), EGCG at a fivefold molar excess prevented membrane aggregation and PI staining, thereby preserving membrane integrity.

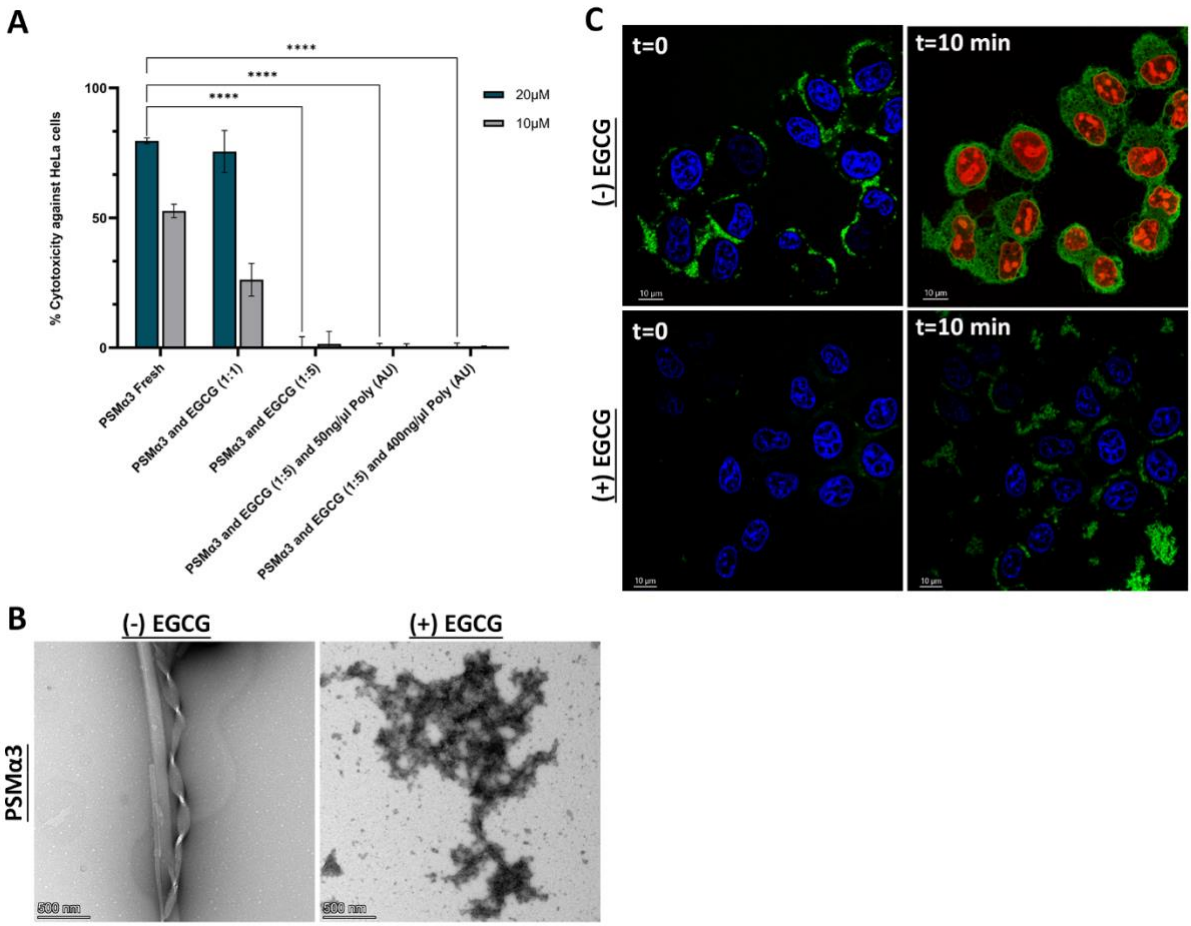

Figure 6. EGCG modulates PSMα3 aggregation and reduces toxicity against HeLa cells. (**A**) Cytotoxicity of PSMα3 against HeLa cells in the presence and absence of EGCG and Poly (AU) RNA at two different concentrations, assessed via LDH assay. The experiment was performed in triplicate and repeated on three separate days for consistency. Cytotoxicity percentages were averaged across all replicates, with error bars representing the standard error of the mean. Statistical significance: *$p < 0.05$, **$p < 0.01$, ***$p < 0.001$, ****$p < 0.0001$ (one-way ANOVA, GraphPad Prism v11). (**B**) TEM micrographs of 100 μM PSMα3 incubated for 24 hours, without (left) and with (right) a fivefold molar excess of EGCG. Scale bars: 500 nm. (**C**) Live-cell confocal microscopy of HeLa cells treated with 20 μM of 20% FITC-PSMα3 (green) and 80% unlabelled PSMα3 without (top) and with EGCG (bottom), imaged immediately after preparation (t = 0) and after 10 minutes. Hoechst 33342 (blue) marks the nuclei, while PI staining (red) indicates membrane disruption. Scale bars: 10 μm.

To investigate residue-specific interactions between PSMα3 and EGCG, we performed NMR spectroscopy using a 2:1 PSMα3:EGCG molar ratio. The 1D 1H-NMR spectrum revealed distinct chemical shift changes and peak broadening upon EGCG addition, particularly in residues Met1, Glu2, and V4/N21, suggesting specific interactions between these sites and the EGCG molecule (Fig. 7A). Peak broadening was also observed in the aromatic region of EGCG, especially for protons H1 and H2, compared to the reference spectrum of EGCG alone, indicating that the interaction is visible from the EGCG side as well. Notably, slight opalescence was observed in the sample following preparation, potentially reflecting early-stage aggregate formation. Additionally, the presence of multiple cross-peaks between non-sequential residues (i+3 or i+4) in the two-dimensional (2D) ^{1}H-^{1}H Nuclear Overhauser Effect Spectroscopy (NOESY) spectrum indicates a well-defined structure of PSMα3 in this condition (Fig. 7B). The 2D ^{1}H-^{1}H Total Correlation Spectroscopy (TOCSY) spectrum displayed connectivity between backbone amide (HN) and alpha protons (Hα) for several assigned residues, while the 2D ^{1}H-^{1}H NOESY spectrum revealed spatial correlations between nearby residues (i+1).

To assess the temporal stability of the sample, we monitored signal intensities over a 3-day period. PSMα3 signals remained stable, with only a ~10% decrease in intensity, whereas EGCG signals exhibited substantial degradation, with nearly 50% loss over the same time frame (Fig. 7C). Given the ~1.5-day duration of the 2D NMR measurements, it is estimated that over 60% of EGCG remained in solution during data acquisition, allowing for reliable observation of its interaction with the peptide. Of note, EGCG's activity has been shown to depend on its chemical stability and the surrounding conditions. Specifically, at neutral pH, EGCG may undergo oxidation, and its inhibitory effects could be attributed to its degradation products rather than the intact compound itself[82].

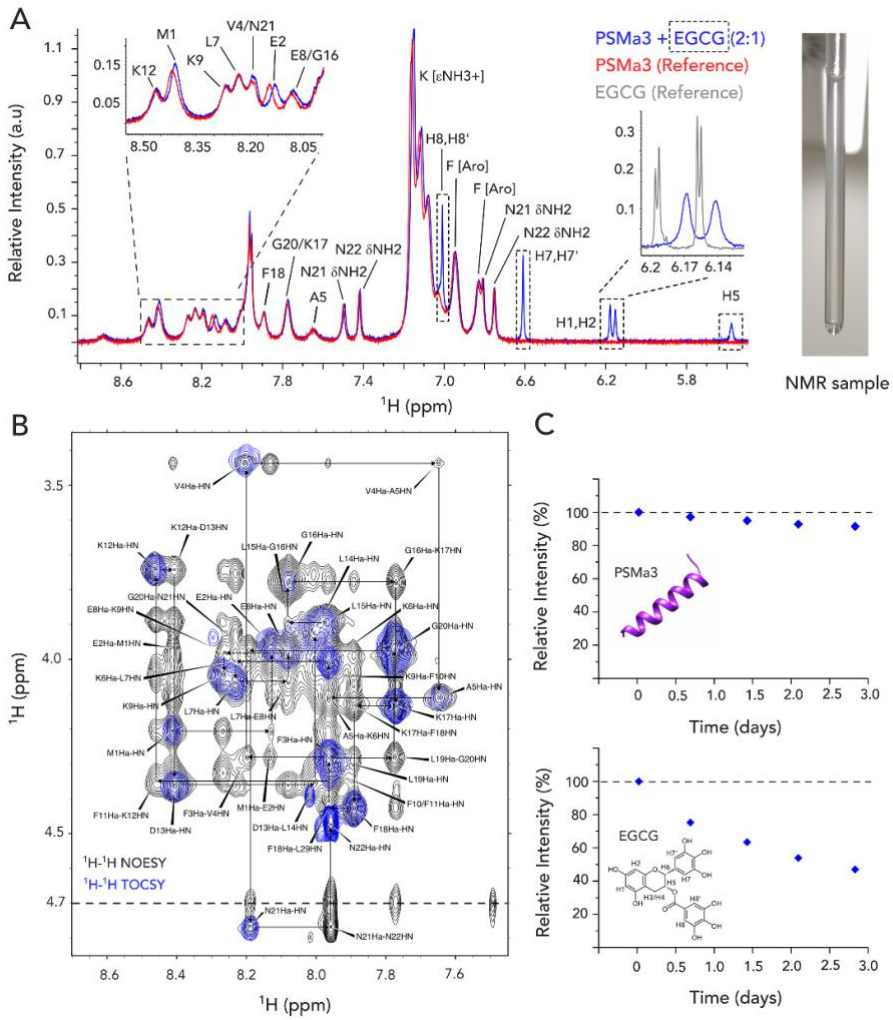

Figure 7. Residue-specific interactions between PSMα3 and EGCG. (**A**) One-dimensional (1D) ^{1}H NMR spectra of 1.0 mM PSMα3 alone (red) and in complex with 0.5 mM EGCG (blue), recorded at 35 °C. Specific residues, including Met1, Glu2 and V4/N21, show chemical shift changes suggestive of direct interaction with EGCG (highlighted in the upper left). Dashed boxes mark proton signals corresponding to EGCG. Peak broadening of H1/H2 protons, compared to the EGCG-only reference sample (light grey), indicates interaction from the EGCG side. Slight opalescence observed in the sample suggests potential aggregate formation. (**B**) Two-dimensional (2D) ^{1}H–^{1}H TOCSY and NOESY spectra of the PSMα3:EGCG complex at a 2:1 ratio, recorded at 35 °C. The cross-peaks in the TOCSY spectrum allow the identification of the spin system and direct connections through the scalar coupling between the proton amide (HN) and the alpha protons (Hα) of the same residue. The cross-peaks in the NOESY spectrum establish a sequential connection between neighbouring residues (i+1), allowing spectral assignment. The remaining cross-peaks (i+3 or i+4) in the spectrum support PSMα3 secondary structure in the experimental conditions. (**C**) Temporal stability of the PSMα3:EGCG sample over 3 days.

RNA modulates the human host defence peptide LL-37 phase behaviour and cytotoxicity without compromising antimicrobial activity

LL-37, a human host defence peptide, shares similarities with PSMα3, including its ability to self-assemble into α-helical supramolecular structures and to interact with nucleic acids[56,65]. We therefore examined whether RNA similarly influences LL-37 activity and properties.

Fluorescence microscopy showed that 100 μM LL-37-FITC incubated with 100 ng/μL PI-labelled Poly (AU) RNA formed aggregates, with no evidence of droplet formation or LLPS under these conditions (Fig. S11). Because diverse cellular stresses are known to induce condensation of RNA-binding proteins and promote the formation of stress-associated assemblies[83], we next examined the effect of RNA on LL-37 under thermal stress. Following heat shock at 65 °C for 15 minutes, RNA markedly altered LL-37 assembly behaviour in a concentration-dependent manner. At 100 ng/μL RNA, LL-37 formed rounded condensates that colocalized with RNA (Fig. 8A). To assess the material properties of these assemblies, we performed FRAP analysis on LL-37–FITC under this condition. Photobleaching resulted in minimal fluorescence recovery over the acquisition window (Fig. S12), indicating that the LL-37–RNA assemblies formed after heat shock are predominantly solid-like rather than liquid-like. At 200 ng/μL RNA, LL-37 assemblies exhibited mixed features, with rounded structures still present but accompanied by increasing aggregation, consistent with a transition toward a more solid state (Fig. 8B). At 400 ng/μL RNA, discrete condensates were no longer observed and LL-37 instead formed extensive, irregular aggregates with strong RNA colocalization (Fig. 8C).

For comparison, PSMα3 subjected to the same heat-shock protocol exhibited droplet formation only under more permissive conditions (pH 4), but not at physiological pH (7.4) (Figs. S13-S14). Together, these results indicate that, for both LL-37 and PSMα3, increasing RNA concentration favours aggregation over phase separation, and that LL-37 assemblies formed

under thermal stress rapidly adopt solid-like properties rather than maintaining liquid-like dynamics.

Freshly dissolved LL-37 exhibited cytotoxicity against HeLa cells, which, in contrast to PSMα3, remained consistent even after incubation for up to 24 hours. Notably, RNA significantly reduced LL-37 cytotoxicity in a concentration-dependent manner, irrespective of the incubation duration (freshly dissolved, 2 hours, or 24 hours) (Fig. 8D). This contrasts with RNA's rescuing effect on the incubation time-dependent loss of PSMα3 cytotoxicity. The antimicrobial activity of LL-37 against *E. coli* also remained unchanged upon incubation. However, unlike its effect on cytotoxicity, RNA had minimal impact on antibacterial activity, with only high concentrations of 400 ng/μL reducing LL-37 activity (Fig. 8E). Similar to PSMα3, LL-37 cytotoxicity against HeLa cells and its antimicrobial activity were attenuated by EGCG in a concentration-dependent manner (Fig. 8E).

TEM micrographs of 100 μM LL-37 revealed a variety of aggregative and fibrous structures, including thin, curli-like fibrils, although no consistent morphology was observed (Fig. S15A). RNA induced a distinct morphological change, leading to increased aggregation and the formation of mostly amorphous species, but also some thicker, ribbon-like fibrils were observed. These structures resemble those previously observed for a segment of the LL-37 active core (residues 17–29), which is similar to PSMα3 in sequence and its ability to form fibrils of densely packed amphipathic α-helices[56]. Heat shock further intensified aggregation, resulting in denser, amorphous condensates and larger fibrillar assemblies, with and without RNA (Fig. S15B). The distinct effects of RNA on the aggregation and morphologies of LL-37 and PSMα3 may underlie the observed differences in their cytotoxic and antibacterial activities.

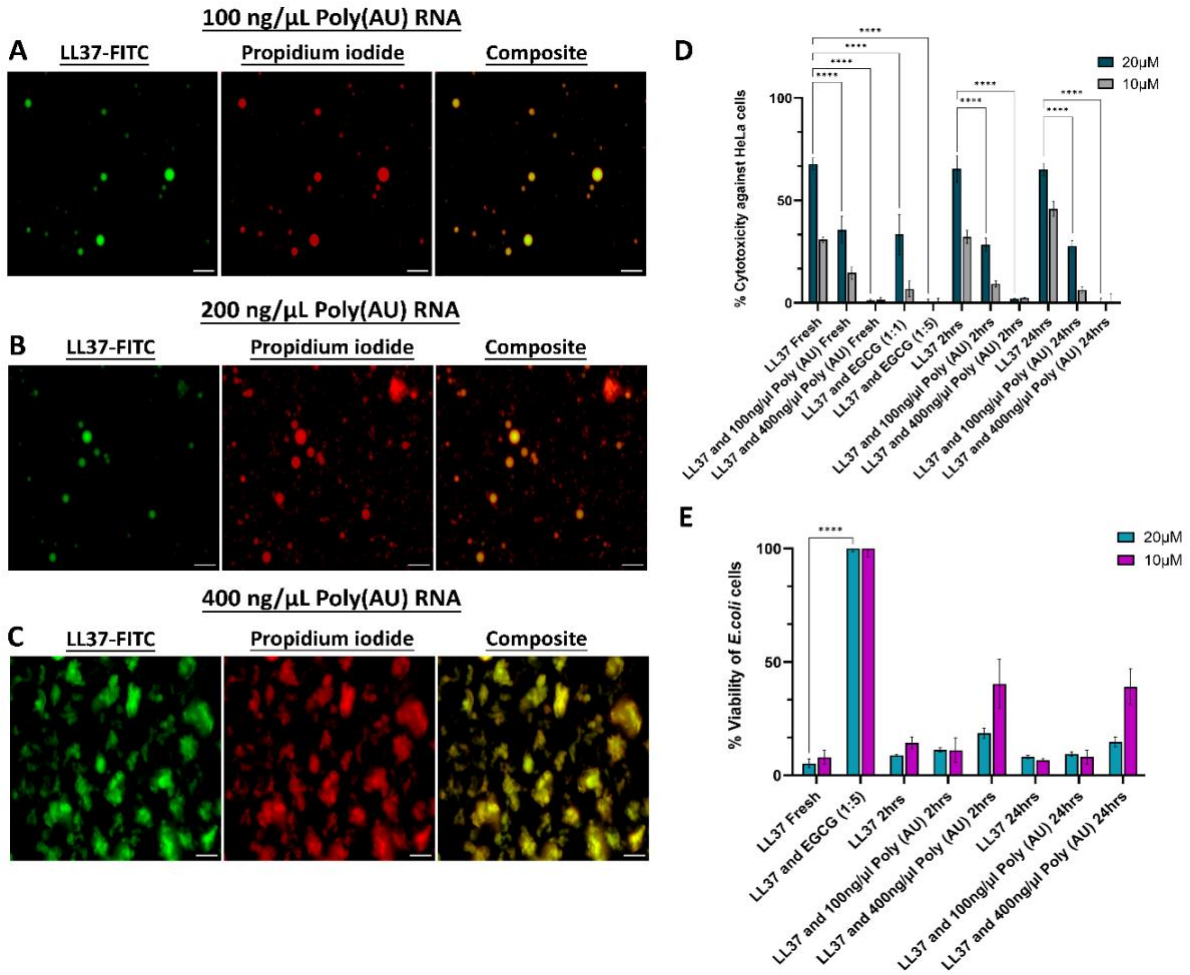

Figure 8. Effect of RNA concentration on LL-37 phase separation, aggregation, and activity at pH 7 after heat shock. Fluorescence microscopy images showing 20% FITC-labelled (green) and 80% unlabelled 100 µM LL-37 in the presence of increasing concentrations: 100 ng/µL (**A**), 200 ng/µL (**B**) and 400 ng/µL (**C**) of Poly (AU) RNA (PI-labelled, red) after heat shock at 65°C for 15 minutes at pH 7. Scale bars represent 20 µm. **(D)** LL-37 cytotoxicity, with and without Poly (AU) RNA and EGCG at varying concentrations, was assessed in HeLa cells using the LDH colorimetric assay. The experiment was performed in triplicate and repeated on three separate days for reproducibility. Cytotoxicity percentages represent the average of all replicates, with error bars indicating the standard error of the mean. **(E)** The antimicrobial activity of LL-37, with and without Poly (AU) RNA and EGCG at varying concentrations, was evaluated against *E. coli* using the PrestoBlue Cell Viability assay. The experiment was performed in triplicate and repeated on three separate days for reproducibility. Bacterial viability percentages represent the average of all replicates, with error bars indicating the standard error of the mean. Statistical significance (**D-E**): *$p < 0.05$, **$p < 0.01$, ***$p < 0.001$, ****$p < 0.0001$ (one-way ANOVA, GraphPad Prism v11).

Discussion

This study identifies RNA as a context-dependent regulator of α-helical assembly-prone peptides, demonstrating that RNA reshapes their supramolecular landscape and thereby tunes bioactivity rather than merely sequestering peptide species. This is supported by the emergence of distinct RNA-dependent material states (from droplets to aged solids) and RNA-dependent fibrillar morphologies with divergent activity profiles across time and concentration. By comparing the bacterial virulence factor PSMα3, which forms canonical cross-α amyloid assemblies, with the human host-defence peptide LL-37, which forms α-helical fibrils but lacks amyloid-like stacking, we reveal that RNA differentially modulates structurally distinct systems through peptide-specific effects on phase behaviour and aggregation dynamics.

Toxicity and antibacterial activity arise from dynamic intermediates

Our data support a model in which PSMα3 toxicity does not arise from a single static species, such as monomers or mature fibrils, but from dynamic assembly processes that include transient α-helical assembly intermediates along the fibrillation pathway. While soluble species mediate cytotoxic activity, mutants that retain α-helical monomeric structure yet fail to fibrillate lose toxicity[14,15], and fully matured fibrils are largely inactive[84,85]. This apparent paradox is resolved by proposing that the toxic window resides within dynamic, membrane-associated assembly intermediates[52]. In this framework, membrane-associated fibril growth may destabilize bilayers through lipid recruitment and extraction[86], analogous to mechanisms proposed for certain human amyloids such as islet amyloid polypeptide[87].

RNA preserves PSMα3 bioactivity by regulating this toxic window and redirecting its assembly pathway

In the absence of RNA, PSMα3 undergoes time-dependent aggregation[31], accompanied by progressive loss of cytotoxic and antimicrobial activity (Fig. 4), coinciding with the formation of dense, fibrillar assemblies (Figs. 2-3). These mature aggregates likely represent inert end states that sequester membrane-active intermediates[84,85]. RNA reshapes this trajectory in a

concentration-dependent manner. At low RNA concentrations, PSMα3 initially retains activity (Fig. 4B) but gradually loses it as liquid-like RNA–PSMα3 condensates mature into more rigid assemblies (Figs. 2-4 & S3), indicating that RNA regulates the lifetime of dynamic intermediates. At higher RNA concentrations, RNA promotes alternative fibrillar polymorphs that retain substantial cytotoxic activity even after prolonged incubation (Fig. 4B). Similarly, RNA preserves antibacterial potency over time (Fig. 4A), consistent with stabilization of assembly states that remain competent for membrane interaction. Thus, RNA does not simply suppress aggregation but modulates the reversibility and supramolecular architecture of α-helical assemblies (Fig. S7), thereby controlling the duration and accessibility of the toxic window.

The temporal differences between cytotoxicity (Fig. 4B) and antibacterial activity (Fig. 4A) may reflect distinct membrane environments, aggregation kinetics, or interactions with bacterial surfaces versus mammalian membranes. Nonetheless, in both contexts, activity correlates with assembly state rather than peptide abundance alone. RNA therefore acts as a structural modulator that controls the lifetime and reversibility of functionally relevant intermediates.

Regulatory modulation versus irreversible inhibition

The contrasting effects of RNA and the amyloid inhibitor EGCG highlight that bioactivity is governed by supramolecular architecture and reversibility rather than aggregation per se. RNA preserves PSMα3 bioactivity by stabilizing dynamic, α-helical assembly states. In contrast, EGCG binds soluble PSMα3 and diverts it into stable amorphous aggregates that represent structural dead ends, abolishing activity (Figs. 6-7). Thus, EGCG should not be viewed as evidence that amyloid fibrils are the toxic species; instead, it abolishes activity by removing/redirecting soluble bioactive species into non-productive amorphous assemblies. Overall, RNA functions as a regulatory modulator of assembly dynamics, whereas EGCG enforces irreversible pathway diversion. These results underscore that assembly state, not simply peptide presence, determines biological function.

LL-37: non-amyloid α-helical assemblies under RNA control

In contrast to PSMα3, LL-37 does not form canonical amyloid architectures. Although it can assemble into α-helical fibrillar structures[53,56], these lack the ordered cross-β or cross-α stacking characteristic of amyloids. Nevertheless, RNA strongly modulates LL-37 behaviour. RNA can selectively attenuate cytotoxicity while preserving antimicrobial function, correlating with the formation of amorphous RNA–LL-37 co-assemblies rather than structured fibrils (Figs. 8, S11 & S15). RNA-dependent condensate-like assemblies are observed only under thermal stress, and these rapidly adopt solid-like properties (Figs. 8 and S12). For LL-37, RNA therefore appears to serve a protective role, minimizing collateral host damage while maintaining immune defence. This suggests that RNA-mediated modulation is a broader principle of α-helical peptide regulation, yet with a functional divergence that may reflect differences in the architecture of the resulting co-assemblies: RNA drives PSMα3 into structured α-helical fibrillar polymorphs, and LL-37 into disordered, amorphous co-aggregates.

Interestingly, although LL-37 does not adopt canonical amyloid architectures, it displays multiple functional connections to amyloid systems. LL-37 has been reported to bind the Alzheimer's-associated amyloid-β (Aβ) peptide and inhibit its fibrillization, likely through stabilization of prefibrillar intermediates[88]. This observation suggests that LL-37 can influence amyloid assembly pathways rather than simply interacting with mature fibrils, with potential implications for aging, immune regulation, and infection. In addition, LL-37 has been shown to interact with human α-synuclein as well as with bacterial curli amyloids, where it modulates biofilm properties[89–91]. Together, these findings position LL-37 as a cross-reactive regulator of amyloid assemblies across host and microbial contexts. The mechanistic basis and physiological relevance of these interactions remain to be further elucidated.

Parallels with phase-transition biology

The dynamic phase transitions observed for PSMα3 mirror those described for human RNA-binding proteins such as FUS, TDP-43, hnRNPA1, and tau, where LLPS enables physiological function but aberrant maturation contributes to neurodegenerative diseases[73,74,92–103].

Antimicrobial peptides can also induce LLPS with nucleic acids and disrupt critical processes like transcription and translation[104]. While the antimicrobial LL-37 is not an amyloid, its RNA-dependent co-assembly behaviour reinforces the broader concept that nucleic acids can regulate peptide phase behaviour across structurally distinct systems.

The nucleolar accumulation of PSMα3 (Fig. 5) is consistent with its intrinsic nucleic acid–binding capacity and provides cellular continuity with the RNA-dependent assemblies observed in vitro (Figs. 2-3). However, given the rapid membrane disruption induced by PSMα3 at cytotoxic concentrations (Figs. 5-6 and Movies S1-S2), nucleolar localization is unlikely to represent a distinct intracellular toxic mechanism. Rather, it reflects binding competence within RNA-rich compartments following cellular entry. The slow and incomplete fluorescence recovery observed in FRAP measurements (Fig. S8) further supports a dynamic yet constrained exchange of PSMα3 within the nucleolus, indicative of interaction with endogenous nucleic acids rather than freely diffusing peptide. The biological relevance of this interaction, particularly at sub-cytotoxic concentrations where membrane disruption does not dominate, remains to be determined and warrants further investigation.

Biological and therapeutic implications

Collectively, these findings position RNA as an environmental regulator of α-helical peptide assemblies, tuning bioactivity by modulating supramolecular organization and reversibility. Nucleic acids are abundant in infection-relevant settings where PSMs operate, including biofilms (rich in extracellular DNA and RNA), abscesses, neutrophil extracellular traps, and damaged tissues that release host RNA. In such contexts, RNA could control the persistence and timing of membrane-active PSM species by shifting assemblies between condensate-like reservoirs and more inert aggregates, thereby modulating virulence without invoking an intracellular mechanism. The divergent outcomes of RNA-mediated modulation-preservation of PSMα3 virulence versus attenuation of LL-37 cytotoxicity thus reflect peptide-specific assembly architectures rather than a uniform effect: RNA sustains dynamic, membrane-competent assemblies for the amyloidogenic PSMα3 while driving the non-amyloidogenic LL-

37 into inactive amorphous states, effectively tilting the host-pathogen balance toward bacterial advantage.

While Poly (AU) served here as a defined, reductionist probe of peptide–RNA interactions, multiple endogenous RNA pools are plausible physiological partners. Within *S. aureus* biofilms, extracellular RNA is an abundant matrix component that contributes structurally to biofilm organization, raising the possibility that it directly modulates PSM assembly and thereby impacts biofilm stability and virulence-factor availability[105,106]. At infection sites, host-derived extracellular RNA released from stressed or dying cells can function as a danger-associated molecular pattern (DAMP)[107,108] and may further shift the balance between PSMα3-driven cytotoxicity and LL-37–mediated host protection within inflammatory milieus. Defining which endogenous RNA species, concentrations, and structural features govern these assembly-dependent effects in vivo is therefore an important next step.

For PSMα3, RNA-sensitive assembly dynamics may provide a means for *S. aureus* to tune virulence in response to local cues, supporting immune evasion, biofilm-associated persistence, and survival across diverse host environments. For LL-37, RNA-mediated attenuation of cytotoxicity without loss of antimicrobial function suggests a host-protective mechanism that helps balance pathogen control with limiting collateral tissue damage. More broadly, this work shifts the conceptual emphasis from amyloid formation as a static endpoint to environmentally regulated phase/assembly transitions and shows that RNA-mediated control extends beyond canonical amyloids to non-amyloid α-helical assemblies. These insights motivate therapeutic strategies aimed at reshaping assembly pathways and material states, rather than simply blocking aggregation.

Methods

Peptide and Poly (AU) RNA preparation

Unlabelled and C-terminal FITC-labelled PSMα3 and LL-37 (PSMα3-FITC and LL-37-FITC) (>98% purity) were purchased from GL Biochem (Shanghai) Ltd. Poly (AU) RNA was purchased from Sigma Aldrich. A stock solution of the peptides was prepared at a concentration of 1 mM in a mixture of 20% dimethyl sulfoxide (DMSO) and 80% ultra-pure water. For light microscopy experiments, we used a mixture of 20% FITC-labelled and 80% unlabelled PSMα3 or LL-37. The Poly (AU) RNA stock solution was prepared at a concentration of 2000 ng/µl in UPW, the stock solution was stored at −80 °C until further use. Labelled Poly (AU) RNA was prepared by introducing 0.02 mg/ml of PI dye to the Poly (AU) RNA stock solution. For the experiments, samples containing 100 µM PSMα3 or LL-37 with Poly (AU) RNA at 10, 50, 100, 200, or 400 ng/µl were prepared in 50 mM HEPES buffer with 150 mM sodium chloride (NaCl), adjusted to pH 7.4, or in 20 µM Tris, 20 µM Bis-Tris, and 20 µM sodium acetate adjusted to pH 4.

Cytotoxicity against HeLa cells tested using the lactate dehydrogenase (LDH) release assay

Human cervical carcinoma HeLa cells (ATCC® CCL-2™) were routinely cultured in Dulbecco's Modified Eagle's Medium - high glucose (DMEM) (Sigma, Israel) with L-glutamine and supplemented with penicillin (100 U/ml), streptomycin (0.1 mg/ml), and with 10% foetal calf serum (Sigma, Israel). The cells grown at 37°C and 5% CO2. One day before the experiment, cells were resuspended in growing medium (DMEM supplemented with 10% foetal calf serum) $1X10^5$ cells/ml. 50 µL of cell suspension were pipetted into a 96-well plate and grown over night. Thirty minutes before the experiment cells were washed and resuspended in 50 µL of DMEM medium supplemented with L-glutamine (100 U/mL), and with penicillin (100 U/mL), streptomycin (0.1 mg/mL), and with 0.5% heat-inactivated foetal calf serum (assay medium). For the cytotoxicity assay, 100 µM PSMα3 was incubated with or without EGCG at molar ratios of 1:1 or 1:5, or with Poly (AU) RNA at concentrations of 50

ng/μL or 400 ng/μL, for the designated incubation times. Similarly, 100 μM LL-37 was prepared under the same conditions, with or without EGCG at 1:1 or 1:5 molar ratios, or Poly (AU) RNA at 100 ng/μL or 400 ng/μL, following the specified incubation times.

Serial two-fold dilutions in assay medium were performed, and 50 μL of each dilution were pipetted into the three different 96-well with the cells. The plates were incubated for 30 min at 37°C and 5% CO2 and then cell lysis was quantified using the LDH release colorimetric assay according to the manufacturer's instructions, including all recommended controls (LDH; Cytotoxicity Detection Kit Plus, Roche Applied Science, Germany). Cell-free assay medium was measured as background. Cells subjected to the same experimental conditions apart from peptide addition were used as a control to account for spontaneous LDH release. Cells subjected to the same experimental conditions apart from peptide addition and treated with manufacturer-supplied lysis buffer were used as a control to account for maximum LDH release. Absorbance at 490 and 690 nm was measured in a plate reader (FLUOstar Omega, BMG Labtech, Germany). Absorbance at 690 nm was subtracted from 490 nm readings to correct for background. The mean absorbance of triplicate samples and controls was calculated, followed by background subtraction. Data was obtained from at least three independent biological replicates, with the arithmetic mean used for averaging. Error bars represent the standard deviation (SD). Statistical analysis, including one-way ANOVA, was performed using GraphPad Prism 10.

Assessment of Bacterial Viability Using PrestoBlue™ HS Cell Viability Reagent

Escherichia coli (E. coli) cultures were grown overnight in Luria Broth (LB) medium at 37 °C with shaking at 220 rpm. PSMα3 and LL-37 stock solutions were prepared by dissolving the peptides at a concentration of 1 mM in a solvent mixture of 20% DMSO and 80% ultra-pure water. From these stock solutions, the following sample preparations were made:

For PSMα3: **(1)**100 μM PSMα3 **(2)**100 μM PSMα3 with 50 ng/μL Poly (AU) RNA **(3)** 100 μM PSMα3 with 400 ng/μL Poly (AU) RNA **(4)** 100 μM PSMα3 with 500 μM EGCG. For LL-37:

(1)100 μM LL-37 **(2)**100 μM LL-37 with 100 ng/μL Poly (AU) RNA **(3)** 100 μM LL-37 with 400 ng/μL Poly (AU) RNA **(4)** 100 μM LL-37 with 500 μM EGCG.

All solutions were prepared in 50 mM HEPES buffer pH 7.4 containing 150 mM NaCl. Where applicable, samples were incubated for the specified durations of 2 hours or 24 hours.

On the day of the experiment, dilutions of the PSMα3 solutions to 20 μM and 10 μM were prepared in LB medium and dispensed into a sterile 96-well black flat-bottom plate (Greiner bio-one). *E. coli* cultures were diluted to an optical density (OD) of 0.2, and bacterial suspensions were added to the wells. The plate was incubated at 37 °C with shaking at 220 rpm for 1 hour to allow the reaction to proceed.

Following incubation, 10X PrestoBlue™ HS Cell Viability Reagent (Invitrogen) was added to the wells. Wells containing only LB medium served as negative controls, while wells containing only *E. coli* served as positive controls. Plates were sealed with a thermal seal film (EXCEL Scientific) and incubated in a plate reader (CLARIOstar). Bacterial viability was assessed using PrestoBlue fluorescence (excitation: 535–560 nm; emission: 590–615 nm) over time. Each condition was tested in triplicate across three independent experiments. Fluorescence values were averaged, and blank readings were subtracted. Antimicrobial activity was determined at the 2-hour time point, when fluorescence was highest in the positive control. Data were obtained from at least three independent biological replicates, with the arithmetic mean used for averaging. Error bars represent the standard deviation (SD). Statistical analysis, including one-way ANOVA, was performed using GraphPad Prism 10.

Transmission electron microscopy (TEM)

For TEM analysis, 4–5 μL of 100 μM PSMα3, with or without EGCG or Poly (AU) RNA at concentrations of 10 ng/μL, 50 ng/μL, and 400 ng/μL, as well as 100 μM LL-37, with or without Poly (AU) RNA at 100 ng/μL and 400 ng/μL, were directly applied onto glow-discharged 400-mesh copper grids (easiGlow; Pelco, Clovis, CA, USA) with a grid hole size of 42 μm, stabilized with Formvar/carbon (Ted Pella, Inc.). The grids were glow-discharged using a 15-mA current

with a negative charge for 25 seconds. Samples were allowed to adhere to the grids for 45 seconds before being stained with a 1% uranyl acetate solution (Electron Microscopy Science, 22400-1) for 45 seconds. The samples were then examined using a ThermoFisher Scientific (FEI) Talos F200C transmission electron microscope, operating at 200 kV and equipped with a Ceta 16M CMOS camera, at the Ilse Katz Institute for Nanoscale Science and Technology, Ben Gurion University of the Negev, Israel.

Turbidity measurements

Turbidity measurements were performed using a FLUOstar Omega plate reader (BMG Labtech) set to a wavelength of 400 nm. For each sample, the protein concentration was maintained at 100 μM, while RNA concentrations were varied across the following levels: 10 ng/μl, 20 ng/μl, 50 ng/μl, 100 ng /μl, 200 ng/μl, and 400 ng/μl. The turbidity of the mixtures was monitored over several hours following resuspension. The maximum absorbance recorded within the first 30 minutes was used as an indicator of the dense phase volume. The experiments were conducted three times with similar observations.

Electrophoretic mobility shift assay (EMSA)

RNA molecules were synthesized by IDT, with oligoA modified by the IRDye 800CW fluorescent dye. Double-stranded RNA was prepared by annealing 10 μM oligoA-IRDye 800CW with 10 μM oligoU in an annealing buffer containing 10 mM Tris-HCl (pH 7.5), 50 mM NaCl, and 1 mM EDTA. The mixture was heated to 95°C for 5 minutes, followed by gradual cooling to 25°C at a rate of 2°C per minute. The final RNA concentration used in the binding reactions was 40 nM (~400ng/μL).

RNA-protein complexes were incubated at 37°C for 30 minutes before being resolved on a 2.5% agarose gel. Gel electrophoresis was performed in a 0.5× TBE buffer for 7 minutes. The complexes were visualized using a Li-Cor Odyssey FC imaging system in the 800 nm channel with a 30-second exposure. For the EMSA, binding reactions were carried out in a buffer composed of 20 mM HEPES (pH 7.9), 50 mM KCl, 1 mM Dithiothreitol (DTT), 0.1 mM

Ethylenediaminetetraacetic acid (EDTA), 5% glycerol, and 0.05% nonyl phenoxypolyethoxylethanol (NP-40). PSMα3 was added to the reactions at final concentrations of 0, 40, 80, 160, and 320 μM. The experiments were conducted three times with similar observations.

Fluorescent microscopy imaging of peptides with RNA in vitro

Prior to imaging, 100 μM PSMα3 or LL-37 (containing 20% FITC-labelled and 80% unlabelled peptide) were combined with PI-labelled Poly (AU) RNA at different concentrations in 50 mM HEPES buffer pH 7.4 containing 150 mM NaCl. Sample were also tested after 65°C heat shock for 15 minutes. In addition, the PSMα3 and RNA mixture was also tested in a different buffer containing 20 μM Tris, 20 μM Bis-Tris, and 20 μM sodium acetate at pH 4 and were subjected to heat shock at 65°C for 15 minutes.

Following preparation, with or without heat shock, a 10 μL aliquot of each sample was transferred to a μ-Slide 8 Well ibidi chamber or to a clean 24 × 60 mm No. 1.5 glass slide for imaging. Fluorescence microscopy was performed using a Leica DMI8 inverted fluorescent microscope equipped with a 63× immersion oil objective (Numerical Aperture, NA = 1.4) at the Life Sciences and Engineering (LS&E) Infrastructure Center, Technion-Israel Institute of Technology, Haifa, Israel. Data were processed and analyzed using Fiji-ImageJ software. The experiment was conducted three times with similar observations.

Fluorescence recovery after photobleaching (FRAP) measurements

FRAP experiments were conducted using a Zeiss LSM 710 laser scanning confocal microscope equipped with a 63× Plan-Apochromat oil immersion objective, NA1.4, at the Life Sciences and Engineering (LS&E) Infrastructure Center, Technion-Israel Institute of Technology, Haifa, Israel. The experiments were performed on condensates from by 100 μM PSMα3 or LL-37 (containing 20% FITC-labelled and 80% unlabelled peptide) mixed with PI-labelled Poly (AU) RNA at various concentrations as indicated in the figures. Photobleaching

was performed using 405 nm and 488 nm laser lines. The experiments were conducted three times with similar observations.

For FRAP analysis inside the nucleolus of HeLa cells, PSMα3 was added to the cells at a final concentration of 20 μM containing 20% FITC-labelled and 80% unlabelled peptide. The cells were incubated with the peptide for 20 minutes before conducting the experiment. Data was processed and analysed using ZEISS ZEN software and Fiji-ImageJ software. The experiments were conducted three times with similar observations.

Total internal reflection fluorescence (TIRF) microscopy

TIRF microscopy was performed using a ZEISS Elyra 7 Super-Resolution Microscope equipped with a 63× Apochromat alpha Plan-Apochromat Oil immersion DIC objective, NA1.46, at the Life Sciences and Engineering (LS&E) Infrastructure Center, Technion-Israel Institute of Technology, Haifa, Israel. Images were acquired using the pco.edge sCMOS cameras, and data were processed and analysed with ZEISS ZEN software to accurately represent the observed phenomena. The condensates and aggregates analysed were generated using 100 μM of 20% FITC-PSMα3 (green) and 80% unlabelled PSMα3 with either 50 ng/μL or 400 ng/μL Poly (AU) RNA. AmyTracker 630 (Ebba Biotech) was added at a 1:500 (peptide: AmyTracker) molar ratio to each sample. The experiments were conducted three times with similar observations.

Confocal microscopy visualization of PSMα3 interaction with HeLa cells

HeLa cells were pre-cultured one day before the experiment by preparing a suspension containing 350,000 cells/ml and plating 150 μl of this suspension into each well of a μ-Slide 8 well glass-bottom chamber. The cells were then incubated overnight under standard growth conditions (37°C, 5% CO2) to allow for adherence and growth. On the day of the experiment, the cells were washed three times with phosphate-buffered saline (PBS) to remove any residual media. Hoechst 33342 dye (10 mg/mL stock) was diluted 1:2000 in fresh cell media and added to the cells. The cells were incubated with Hoechst for 10 minutes at 37°C and 5%

CO2. After incubation, cells were washed three times with PBS to remove Hoechst residuals. A working solution of PI was prepared by diluting a 1 mg/ml PI stock solution to a final concentration of 0.02 mg/ml in fresh cell growth media. Immediately prior to imaging, PSMα3 was added to the cells at a final concentration of 20 μM containing 20% FITC-labelled and 80% unlabelled peptide. The cells were then imaged using a Ti2-E microscope by Nikon with a CSU-W1 spinning disk confocal unit by Yokogawa, equipped with a 100X CFI SR HP Plan Apochromat Lambda S silicone immersion objective, NA1.35, at the Life Sciences and Engineering (LS&E) Infrastructure Center, Technion-Israel Institute of Technology, Haifa, Israel. Confocal movies and images were captured by Photometrics BSI sCMOS cameras to observe the interaction and localization of PSMα3 within the cells, focusing particularly on its colocalization with nucleic acids in the nucleolar region. The acquired images and movies were subsequently analysed using Imaris Image Analysis Software (Oxford Instruments). The experiments were conducted three times with similar observations.

Super resolution light microscopy visualization of PSMα3 interaction with *E. coli*

E. coli lptD4213 cells were a kind gift from Prof. Sima Yaron from the Technion – Israel Institute of Technology. An inoculum was pre-cultured in Luria-Bertani medium (LB) medium at 220 rpm and 37°C for 24 hours prior to the experiment. On the day of the experiment, the optical density (OD) of the culture was measured, and the cells were diluted to an OD of 0.4. The cells were then incubated with 20 μM of 20% FITC-PSMα3 (green) and 80% unlabelled PSMα3, with and without EGCG at 1:5 molar ratio, alongside a bacteria-only control. Samples were incubated for 30 minutes at 220 rpm and 37°C. Following incubation, the samples were centrifuged three times for 3 minutes at 1.5g, with the supernatant discarded and the pellet resuspended in 1X PBS after each spin. The resuspended cells were then stained with 50 μg/mL wheat germ agglutinin (WGA) CF633 for 30 minutes. After staining, the cells were washed three times by centrifugation with PBS to remove excess WGA. During the final wash, the cells were resuspended in 0.1 mg/mL PI solution.

Prior to imaging, the samples were loaded into an ibidi μ-Slide VI 0.4. Imaging was performed using a ZEISS Elyra 7 Super-Resolution Microscope equipped with a 63× Apochromat alpha Plan-Apochromat Oil immersion DIC objective, NA 1.4, and pco.edge sCMOS cameras. Lattice structured illumination images were acquired and processed using the ZEN black software at the Life Sciences and Engineering (LS&E) Infrastructure Center, Technion-Israel Institute of Technology, Haifa, Israel. The experiments were conducted three times with similar observations.

Thioflavin T fluorescence fibrillation kinetics assay

Thioflavin T (ThT) (Sigma Aldrich) is a widely used fluorescent dye for detecting and analyzing amyloid fibril formation kinetics. Fibrillation curves in the presence of ThT typically exhibit an initial lag phase followed by rapid fibril elongation. To accurately capture the fibrillation lag time, PSMα3 was pre-treated before the experiment. The peptide was dissolved in a 1:1 mixture of 1,1,1,3,3,3-Hexafluoroisopropanol (HFIP- Sigma Aldrich) and Trifluoroacetic acid (TFA- Sigma Aldrich) to a final concentration of 1 mg/mL, followed by bath sonication for 10 minutes at room temperature. The organic solvents were then evaporated using a mini-rotational vacuum concentrator (Christ, Germany) at 1,000 rpm for 2 hours at room temperature.

For the experiment, freshly prepared 100 μM PSMα3 peptides, with or without 500 μM Epigallocatechin gallate (EGCG) at a 1:5 molar ratio, were prepared in 50 mM HEPES buffer pH 7.4 containing 150 mM NaCl. ThT was prepared by diluting a stock solution in ultrapure double-distilled water (UPddw) and filtered before use to reach a final concentration of 200 μM Blank control solutions containing all components except for the peptide were prepared for each reaction.

The assay was conducted in black 96-well flat-bottom plates (Greiner Bio-One), which were sealed with a thermal seal film (EXCEL Scientific) to prevent evaporation. Samples were incubated in a plate reader (OMEGA) at 37°C, shaking at 500 rpm for 85 seconds before each reading cycle, for up to 1,000 cycles of 6 minutes each, totalling approximately 100 hours.

Fluorescence was measured in triplicate using an excitation wavelength of 438 ± 20 nm and an emission wavelength of 490 ± 20 nm. All values were averaged, background fluorescence was subtracted using blank controls, and the results were plotted over time. Standard error of the mean is shown as error bars. The entire experiment was independently repeated at least three times on different days to ensure reproducibility.

Solid-State Circular Dichroism Spectroscopy

Solid-state circular dichroism spectroscopy(ss-CD) was conducted with PSMa3 to assess their fibrillar secondary structure components in presence and absence of Poly (AU) RNA. For preparation of peptide and RNA samples, see Peptide and Poly (AU) preparation section. PSMa3 was prepared at a working concentration of 100 µM in 50 mM HEPES, pH 7.4, 150 mM NaCl at 0 ng/µL, 50 ng/µL or 400 ng/µL Poly (AU) RNA. The reaction mixes were incubated for 0 min, 2 h and 72 h at 37 °C in a non-shaking thermocycler. Following incubation, soluble reaction components were removed via dilution washing with 150 µL water and centrifugation at 12.500 rcf for 30 min. 20 µL of the sediment were resuspended in 180 µL water for a second washing centrifugation step at 12.500 rcf for 30 min. 180 µL of the supernatant were discarded and 18 µL of sediment applied to a *Chirascan Series fused silica disc* (AP/CSSD, Applied Photophysics) in three times 6 µL steps. After every sample application onto to the silica disc, all liquid was evaporated at 37 °C for 5–10 min until only an opaque film remained visible. For secondary structure determination of aggregated/fibrillar peptide components on the silica disc, the disc was inserted into a *Chirascan solid sample holder* (CS/SSH, Applied Photophysics) and the circular dichroism recorded in the far-UV (180–250 nm, step size 1 nm, time-per-point 1 s) using a CD spectropolarimeter (Applied Photophysics). To counteract sample anisotropy, CD spectra were recorded at least four different disc rotations and the results averaged. Prior to data analysis, silica disc and buffer/water backgrounds were subtracted from recorded sample spectra. Poly (AU) RNA-only background spectra showed complex and high amplitude signals that did not appear for samples in combination with peptides and were therefore not subtracted from sample spectra.

NMR experiments

To prepare the reference samples for NMR analysis, 0.521 mg of PSMα3 was dissolved in 180 µL of 20 mM MES (2-(N-morpholino)ethanesulfonic acid) buffer at pH 6.0, supplemented with 5% (v/v) deuterium oxide (D_2O). From this solution, 170 µL was transferred into a 3.0 mm NMR tube for spectral acquisition. In parallel, a 4 mM stock solution of EGCG was prepared in the same 20 mM MES buffer (pH 6.0). From this, a working solution containing 0.5 mM EGCG in 20 mM MES with 5% (v/v) D_2O was prepared to match the buffer conditions of the peptide sample. A volume of 170 µL was then transferred into a separate 3.0 mm NMR tube for use as the EGCG reference.

All NMR experiments were recorded on a Bruker 700 MHz spectrometer equipped with a triple-resonance cryoprobe (Prodigy) and an AVANCE NEO console. One-dimensional (1D) ^{1}H-NMR spectra were acquired using the Bruker library pulse sequence zggpw5 for water suppression. The acquisition parameters were: acquisition time (AQ) = 1.90 s, spectral width (SW) = 12.31 ppm, recovery delay (D1) = 1.5 s, and 64 scans. All experiments were conducted at 35 °C, under which optimal spectral quality was obtained.

Two-dimensional (2D) ^{1}H–^{1}H TOCSY (Total Correlation Spectroscopy) spectra were collected using the Bruker pulse sequence dipsi2gpph19. Acquisition parameters were: t_2 = 2048 complex points (AQ_2 = 0.118 s), t_1 = 512 complex points (AQ_1 = 0.029 s), SW_1 = SW_2 = 12.31 ppm, with 64 scans and a mixing time (tmix) of 80 ms. Recovery delay (D1) was set to 1.5 s. 2D ^{1}H–^{1}H NOESY (Nuclear Overhauser Effect Spectroscopy) spectra were acquired using the noesyfpgpph19 pulse sequence, with acquisition parameters identical to those used for TOCSY. The mixing time was set to 300 ms. Total experimental time for the combined 2D TOCSY and NOESY experiments was approximately 30 hours. NMR data processing was carried out using TopSpin 4.5.0 (Bruker), and spectral assignments for the 2D TOCSY and NOESY spectra were performed using POKY software[68]. Signal integration was carried out using in-house scripts written in Scilab[69].

Data availability

Raw data is also deposited in: https://doi.org/10.5281/zenodo.17598867

Acknowledgements

M.L. acknowledges research support from the Israel Science Foundation, Grant No. 2111/20 and the Cure Alzheimer's Fund. M.L. and M.Z. acknowledge the Forschungskooperation Niedersachsen – Israel, Volkswagenstiftung, No: 76251-4659/2022 (ZN 4042). Funded/Co-funded by the European Union (ERC, FuncAmyloid, 101087140). Views and opinions expressed are however those of the author(s) only and do not necessarily reflect those of the European Union or the European Research Council. Neither the European Union nor the granting authority can be held responsible for them. A.K.B thanks the Novo Nordisk Foundation (Grant number NNFSA17002839) and the European Union (ERC CoG 101088163 EMMA) for funding. We thank Ayala Shiber for advice and guidance, as well as Yael Mandel-Gutfreund and Hiba Hassanain for their assistance with RNA preparations. We acknowledge guidance and support from Nitsan Dahan from the Microscopy core facility center at the Lorry I. Lokey Interdisciplinary Center for Life Sciences and Engineering. We acknowledge the use of OpenAI's GPT-4 and other AI-based models to improve the writing quality of parts of this manuscript.

References

1. Barnhart, M. M. & Chapman, M. R. Curli biogenesis and function. *Annu Rev Microbiol* **60**, 131–147 (2006).

2. Sleutel, M., Pradhan, B., Volkov, A. N. & Remaut, H. Structural analysis and architectural principles of the bacterial amyloid curli. *Nat Commun* **14**, 2822 (2023).

3. Howard, M. K. *et al.* Probing the drivers of Staphylococcus aureus biofilm protein amyloidogenesis and disrupting biofilms with engineered protein disaggregases. *mBio* **14**, e00587-23 (2023).

4. Salinas, N., Povolotsky, T. L., Landau, M. & Kolodkin-Gal, I. Emerging Roles of Functional Bacterial Amyloids in Gene Regulation, Toxicity, and Immunomodulation. *Microbiol Mol Biol Rev* **85**, e00062-20 (2020).

5. Van Gerven, N., Van der Verren, S. E., Reiter, D. M. & Remaut, H. The Role of Functional Amyloids in Bacterial Virulence. *J Mol Biol* **430**, 3657–3684 (2018).

6. Peña-Díaz, S., Olsen, W. P., Wang, H. & Otzen, D. E. Functional Amyloids: The Biomaterials of Tomorrow? *Adv Mater* **36**, e2312823 (2024).

7. Chapman, M. R. *et al.* Role of Escherichia coli curli operons in directing amyloid fiber formation. *Science* **295**, 851–855 (2002).

8. Blanco, L. P., Evans, M. L., Smith, D. R., Badtke, M. P. & Chapman, M. R. Diversity, biogenesis and function of microbial amyloids. *Trends Microbiol* **20**, 66–73 (2012).

9. Perov, S. *et al.* Structural Insights into Curli CsgA Cross-β Fibril Architecture Inspire Repurposing of Anti-amyloid Compounds as Anti-biofilm Agents. *PLoS Pathog* **15**, e1007978 (2019).

10. Golan, N. *et al.* Resilience and charge-dependent fibrillation of functional amyloid: Interactions of Pseudomonas biofilm-associated FapB and FapC amyloids. *J Biol Chem* **301**, 108096 (2025).

11. Jiang, Y. *et al.* Natural Design of a Stabilized Cross-β Fold: Structure of the FuA FapC from Pseudomonas Sp. UK4 Reveals a Critical Role for Stacking of Imperfect Repeats. *Adv Mater* **37**, e2505503 (2025).

12. Schwartz, K., Syed, A. K., Stephenson, R. E., Rickard, A. H. & Boles, B. R. Functional amyloids composed of phenol soluble modulins stabilize Staphylococcus aureus biofilms. *PLoS Pathog* **8**, e1002744 (2012).

13. Schwartz, K. *et al.* The AgrD N-Terminal Leader Peptide of Staphylococcus aureus Has Cytolytic and Amyloidogenic Properties. *Infection and Immunity* **82**, 3837–3844 (2014).

14. Tayeb-Fligelman, E., Salinas, N., Tabachnikov, O. & Landau, M. Staphylococcus aureus PSMα3 Cross-α Fibril Polymorphism and Determinants of Cytotoxicity. *Structure* **28**, 301-313.e6 (2020).

15. Tayeb-Fligelman, E. *et al.* The cytotoxic Staphylococcus aureus PSMα3 reveals a cross-α amyloid-like fibril. *Science* **355**, 831–833 (2017).

16. Kreutzberger, M. A. B. *et al.* Phenol-soluble modulins PSMα3 and PSMβ2 form nanotubes that are cross-α amyloids. *Proc Natl Acad Sci U S A* **119**, e2121586119 (2022).

17. Schwartz, K. & Boles, B. R. Microbial amyloids--functions and interactions within the host. *Curr Opin Microbiol* **16**, 93–99 (2013).

18. Zhou, X. *et al.* Staphylococcus aureus N-terminus formylated δ-toxin tends to form amyloid fibrils, while the deformylated δ-toxin tends to form functional oligomer complexes. *Virulence* **12**, 1418–1437 (2021).

19. Hansen, K. H. *et al.* Structure of biofilm-forming functional amyloid PSMα1 from Staphylococcus aureus. *Proc Natl Acad Sci U S A* **121**, e2406775121 (2024).

20. Wang, X. *et al.* Staphylococcus aureus delta toxin modulates both extracellular membrane vesicle biogenesis and amyloid formation. *mBio* **14**, e0174823 (2023).

21. Mehlin, C., Headley, C. M. & Klebanoff, S. J. An Inflammatory Polypeptide Complex from Staphylococcus epidermidis: Isolation and Characterization. *J Exp Med* **189**, 907–918 (1999).

22. Chatterjee, S. S. *et al.* Essential Staphylococcus aureus toxin export system. *Nat Med* **19**, 364–367 (2013).

23. Kretschmer, D. *et al.* Human formyl peptide receptor 2 senses highly pathogenic Staphylococcus aureus. *Cell Host Microbe* **7**, 463–473 (2010).

24. Queck, S. Y. *et al.* Mobile Genetic Element-Encoded Cytolysin Connects Virulence to Methicillin Resistance in MRSA. *PLoS Pathog* **5**, e1000533 (2009).

25. Joo, H.-S. & Otto, M. Molecular basis of in vivo biofilm formation by bacterial pathogens. *Chem Biol* **19**, 1503–1513 (2012).

26. Hu, Z. *et al.* Phenol-soluble modulin α and β display divergent roles in mice with staphylococcal septic arthritis. *Commun Biol* **5**, 1–11 (2022).

27. Grando, K. *et al.* Phenol-Soluble Modulins From Staphylococcus aureus Biofilms Form Complexes With DNA to Drive Autoimmunity. *Front Cell Infect Microbiol* **12**, 884065 (2022).

28. Cheung, G. Y. C., Joo, H.-S., Chatterjee, S. S. & Otto, M. Phenol-soluble modulins--critical determinants of staphylococcal virulence. *FEMS Microbiol Rev* **38**, 698–719 (2014).

29. Arad, E. *et al.* Staphylococcus aureus functional amyloids catalyze degradation of β-lactam antibiotics. *Nat Commun* **14**, 8198 (2023).

30. Zaman, M. & Andreasen, M. Cross-talk between individual phenol-soluble modulins in Staphylococcus aureus biofilm enables rapid and efficient amyloid formation. *eLife* **9**, e59776 (2020).

31. Rayan, B., Barnea, E., Khokhlov, A., Upcher, A. & Landau, M. Differential fibril morphologies and thermostability determine functional roles of Staphylococcus aureus PSMα1 and PSMα3. *Front Mol Biosci* **10**, 1184785 (2023).

32. Marinelli, P., Pallares, I., Navarro, S. & Ventura, S. Dissecting the contribution of Staphylococcus aureus α-phenol-soluble modulins to biofilm amyloid structure. *Sci Rep* **6**, 34552 (2016).

33. Le, K. Y., Dastgheyb, S., Ho, T. V. & Otto, M. Molecular determinants of staphylococcal biofilm dispersal and structuring. *Front Cell Infect Microbiol* **4**, 167 (2014).

34. Peschel, A. & Otto, M. Phenol-soluble modulins and staphylococcal infection. *Nat Rev Microbiol* **11**, 667–673 (2013).

35. Mehlin, C., Headley, C. M. & Klebanoff, S. J. An Inflammatory Polypeptide Complex from Staphylococcus epidermidis: Isolation and Characterization. *J Exp Med* **189**, 907–918 (1999).

36. Chatterjee, S. S. *et al.* Essential Staphylococcus aureus toxin export system. *Nat Med* **19**, 364–367 (2013).

37. Seuring, C. *et al.* The three-dimensional structure of human β-endorphin amyloid fibrils. *Nat Struct Mol Biol* **27**, 1178–1184 (2020).

38. Banerjee, P. R., Milin, A. N., Moosa, M. M., Onuchic, P. L. & Deniz, A. A. Reentrant Phase Transition Drives Dynamic Substructure Formation in Ribonucleoprotein Droplets. *Angew Chem Int Ed Engl* **56**, 11354–11359 (2017).

39. Morelli, C. *et al.* RNA modulates hnRNPA1A amyloid formation mediated by biomolecular condensates. *Nat Chem* **16**, 1052–1061 (2024).

40. Cheung, G. Y. C. *et al.* Insight into structure-function relationship in phenol-soluble modulins using an alanine screen of the phenol-soluble modulin (PSM) α3 peptide. *FASEB J* **28**, 153–161 (2014).

41. Wang, R. *et al.* Identification of novel cytolytic peptides as key virulence determinants for community-associated MRSA. *Nat Med* **13**, 1510–1514 (2007).

42. Laabei, M., Jamieson, W. D., Yang, Y., van den Elsen, J. & Jenkins, A. T. A. Investigating the lytic activity and structural properties of Staphylococcus aureus phenol soluble modulin (PSM) peptide toxins. *Biochim Biophys Acta* **1838**, 3153–3161 (2014).

43. Ragonis-Bachar, P. *et al.* Natural Antimicrobial Peptides Self-assemble as α/β Chameleon Amyloids. *Biomacromolecules* **23**, 3713–3727 (2022).

44. Salinas, N. *et al.* The amphibian antimicrobial peptide uperin 3.5 is a cross-α/cross-β chameleon functional amyloid. *Proc Natl Acad Sci U S A* **118**, e2014442118 (2021).

45. Bücker, R. *et al.* The Cryo-EM structures of two amphibian antimicrobial cross-β amyloid fibrils. *Nat Commun* **13**, 4356 (2022).

46. Strati, F. *et al.* Structural and Functional Versatility of the Amyloidogenic Non-Amidated Variant of the Antimicrobial Peptide Citropin 1.3. *Adv Sci (Weinh)* **12**, e03997 (2025).

47. Landau, M. *et al.* Expanding the amyloid landscape: structural plasticity of antimicrobial peptides. Preprint at https://doi.org/10.21203/rs.3.rs-8249669/v1 (2026).

48. Tempra, C., La Rosa, C. & Lolicato, F. The role of alpha-helix on the structure-targeting drug design of amyloidogenic proteins. *Chem Phys Lipids* **236**, 105061 (2021).

49. Ramamoorthy, A. & Lim, M. H. Structural characterization and inhibition of toxic amyloid-β oligomeric intermediates. *Biophys J* **105**, 287–288 (2013).

50. Ghosh, D. *et al.* Structure based aggregation studies reveal the presence of helix-rich intermediate during α-Synuclein aggregation. *Sci Rep* **5**, 9228 (2015).

51. Salinas, N., Colletier, J.-P., Moshe, A. & Landau, M. Extreme amyloid polymorphism in Staphylococcus aureus virulent PSMα peptides. *Nat Commun* **9**, 3512 (2018).

52. Cali, M. P. *et al.* The Many Lives of a Single Sequence: Functional Plasticity Through Amyloid Polymorphism. *Subcell Biochem* **113**, 521–558 (2026).

53. Sancho-Vaello, E. *et al.* The structure of the antimicrobial human cathelicidin LL-37 shows oligomerization and channel formation in the presence of membrane mimics. *Sci Rep* **10**, 17356 (2020).

54. Zeth, K. & Sancho-Vaello, E. Structural Plasticity of LL-37 Indicates Elaborate Functional Adaptation Mechanisms to Bacterial Target Structures. *Int J Mol Sci* **22**, 5200 (2021).

55. Porcelli, F. *et al.* NMR structure of the cathelicidin-derived human antimicrobial peptide LL-37 in dodecylphosphocholine micelles. *Biochemistry* **47**, 5565–5572 (2008).

56. Engelberg, Y. & Landau, M. The Human LL-37(17-29) antimicrobial peptide reveals a functional supramolecular structure. *Nat Commun* **11**, 3894 (2020).

57. Rumpret, M. *et al.* Signal inhibitory receptor on leukocytes-1 recognizes bacterial and endogenous amphipathic α-helical peptides. *FASEB J* **35**, e21875 (2021).

58. Golan, N., Engelberg, Y. & Landau, M. Structural Mimicry in Microbial and Antimicrobial Amyloids. *Annual Review of Biochemistry* **91**, 403–422 (2022).

59. Rautenberg, M., Joo, H.-S., Otto, M. & Peschel, A. Neutrophil responses to staphylococcal pathogens and commensals via the formyl peptide receptor 2 relates to phenol-soluble modulin release and virulence. *FASEB J* **25**, 1254–1263 (2011).

60. Syed, A. K., Reed, T. J., Clark, K. L., Boles, B. R. & Kahlenberg, J. M. Staphlyococcus aureus phenol-soluble modulins stimulate the release of proinflammatory cytokines from keratinocytes and are required for induction of skin inflammation. *Infect Immun* **83**, 3428–3437 (2015).

61. Schreiner, J. *et al.* Staphylococcus aureus phenol-soluble modulin peptides modulate dendritic cell functions and increase in vitro priming of regulatory T cells. *J Immunol* **190**, 3417–3426 (2013).

62. Chu, M. *et al.* Staphylococcus aureus Phenol-Soluble Modulins α1-α3 Act as Novel Toll-Like Receptor (TLR) 4 Antagonists to Inhibit HMGB1/TLR4/NF-κB Signaling Pathway. *Front Immunol* **9**, 862 (2018).

63. Kretschmer, D., Nikola, N., Dürr, M., Otto, M. & Peschel, A. The Virulence Regulator Agr Controls the Staphylococcal Capacity to Activate Human Neutrophils via the Formyl Peptide Receptor 2. *J Innate Immun* **4**, 201–212 (2012).

64. Bröker, B. M., Mrochen, D. & Péton, V. The T Cell Response to Staphylococcus aureus. *Pathogens* **5**, 31 (2016).

65. Ganguly, D. *et al.* Self-RNA-antimicrobial peptide complexes activate human dendritic cells through TLR7 and TLR8. *J Exp Med* **206**, 1983–1994 (2009).

66. Lee, E. Y. *et al.* Crystallinity of Double-Stranded RNA-Antimicrobial Peptide Complexes Modulates Toll-Like Receptor 3-Mediated Inflammation. *ACS Nano* **11**, 12145–12155 (2017).

67. Tewary, P. *et al.* β-Defensin 2 and 3 promote the uptake of self or CpG DNA, enhance IFN-α production by human plasmacytoid dendritic cells, and promote inflammation. *J Immunol* **191**, 865–874 (2013).

68. Schmidt, N. W. *et al.* Liquid-crystalline ordering of antimicrobial peptide-DNA complexes controls TLR9 activation. *Nat Mater* **14**, 696–700 (2015).

69. Lee, E. Y. *et al.* Helical antimicrobial peptides assemble into protofibril scaffolds that present ordered dsDNA to TLR9. *Nat Commun* **10**, 1012 (2019).

70. Tursi, S. A. *et al.* Bacterial amyloid curli acts as a carrier for DNA to elicit an autoimmune response via TLR2 and TLR9. *PLOS Pathogens* **13**, e1006315 (2017).

71. Gallo, P. M. *et al.* Amyloid-DNA Composites of Bacterial Biofilms Stimulate Autoimmunity. *Immunity* **42**, 1171–1184 (2015).

72. Alberti, S., Gladfelter, A. & Mittag, T. Considerations and Challenges in Studying Liquid-Liquid Phase Separation and Biomolecular Condensates. *Cell* **176**, 419–434 (2019).

73. Aa, H., Ca, W. & F, J. Liquid-liquid phase separation in biology. *Annual review of cell and developmental biology* **30**, (2014).

74. B, W. *et al.* Liquid-liquid phase separation in human health and diseases. *Signal transduction and targeted therapy* **6**, (2021).

75. Xu, Z., Wang, W., Cao, Y. & Xue, B. Liquid-liquid phase separation: Fundamental physical principles, biological implications, and applications in supramolecular materials engineering. *Supramolecular Materials* **2**, 100049 (2023).

76. Indig, R. Y. & Landau, M. Designed inhibitors to reduce amyloid virulence and cytotoxicity and combat neurodegenerative and infectious diseases. *Current Opinion in Chemical Biology* **75**, 102318 (2023).

77. Fernandes, L., Cardim-Pires, T. R., Foguel, D. & Palhano, F. L. Green Tea Polyphenol Epigallocatechin-Gallate in Amyloid Aggregation and Neurodegenerative Diseases. *Front Neurosci* **15**, 718188 (2021).

78. Andrich, K. & Bieschke, J. The Effect of (-)-Epigallo-catechin-(3)-gallate on Amyloidogenic Proteins Suggests a Common Mechanism. *Adv Exp Med Biol* **863**, 139–161 (2015).

79. Nott, T. J. *et al.* Phase Transition of a Disordered Nuage Protein Generates Environmentally Responsive Membraneless Organelles. *Mol Cell* **57**, 936–947 (2015).

80. Amico, T. *et al.* A scale-invariant log-normal droplet size distribution below the critical concentration for protein phase separation. *Elife* **13**, RP94214 (2024).

81. Ray, S. & Buell, A. K. Emerging experimental methods to study the thermodynamics of biomolecular condensate formation. *J Chem Phys* **160**, 091001 (2024).

82. Sternke-Hoffmann, R., Peduzzo, A., Bolakhrif, N., Haas, R. & Buell, A. K. The Aggregation Conditions Define Whether EGCG is an Inhibitor or Enhancer of α-Synuclein Amyloid Fibril Formation. *Int J Mol Sci* **21**, 1995 (2020).

83. Riback, J. A. *et al.* Stress-Triggered Phase Separation Is an Adaptive, Evolutionarily Tuned Response. *Cell* **168**, 1028-1040.e19 (2017).

84. Zheng, Y., Joo, H.-S., Nair, V., Le, K. Y. & Otto, M. Do amyloid structures formed by Staphylococcus aureus phenol-soluble modulins have a biological function? *Int J Med Microbiol* **308**, 675–682 (2018).

85. Yao, Z. *et al.* Use of a Stereochemical Strategy To Probe the Mechanism of Phenol-Soluble Modulin α3 Toxicity. *J Am Chem Soc* **141**, 7660–7664 (2019).

86. Malishev, R. *et al.* Reciprocal Interactions between Membrane Bilayers and S. aureus PSMα3 Cross-α Amyloid Fibrils Account for Species-Specific Cytotoxicity. *J Mol Biol* **430**, 1431–1441 (2018).

87. Sparr, E. *et al.* Islet amyloid polypeptide-induced membrane leakage involves uptake of lipids by forming amyloid fibers. *FEBS Lett* **577**, 117–120 (2004).

88. De Lorenzi, E. *et al.* Evidence that the Human Innate Immune Peptide LL-37 may be a Binding Partner of Amyloid-β and Inhibitor of Fibril Assembly. *J Alzheimers Dis* **59**, 1213–1226 (2017).

89. Kai-Larsen, Y. *et al.* Uropathogenic Escherichia coli Modulates Immune Responses and Its Curli Fimbriae Interact with the Antimicrobial Peptide LL-37. *PLOS Pathogens* **6**, e1001010 (2010).

90. Santos, J., Ventura, S. & Pallarès, I. LL-37 and CsgC exemplify the crosstalk between anti-amyloid, antimicrobial, and anti-biofilm protein activities. *Neural Regen Res* **18**, 1027–1028 (2023).

91. Santos, J. *et al.* α-Helical peptidic scaffolds to target α-synuclein toxic species with nanomolar affinity. *Nat Commun* **12**, 3752 (2021).

92. Murakami, T. *et al.* ALS/FTD Mutation-Induced Phase Transition of FUS Liquid Droplets and Reversible Hydrogels into Irreversible Hydrogels Impairs RNP Granule Function. *Neuron* **88**, 678–690 (2015).

93. Wang, Y.-L. *et al.* Liquid-liquid phase separation in DNA double-strand breaks repair. *Cell Death Dis* **14**, 1–10 (2023).

94. Kanaan, N. M., Hamel, C., Grabinski, T. & Combs, B. Liquid-liquid phase separation induces pathogenic tau conformations in vitro. *Nat Commun* **11**, 2809 (2020).

95. Ambadipudi, S., Biernat, J., Riedel, D., Mandelkow, E. & Zweckstetter, M. Liquid–liquid phase separation of the microtubule-binding repeats of the Alzheimer-related protein Tau. *Nat Commun* **8**, 275 (2017).

96. Boyko, S. & Surewicz, W. K. Tau liquid-liquid phase separation in neurodegenerative diseases. *Trends Cell Biol* **32**, 611–623 (2022).

97. Wegmann, S. *et al.* Tau protein liquid–liquid phase separation can initiate tau aggregation. *The EMBO Journal* https://doi.org/10.15252/embj.201798049 (2018) doi:10.15252/embj.201798049.

98. Babinchak, W. M. *et al.* The role of liquid–liquid phase separation in aggregation of the TDP-43 low-complexity domain. *Journal of Biological Chemistry* **294**, 6306–6317 (2019).

99. Mukherjee, S., Poudyal, M., Dave, K., Kadu, P. & Maji, S. K. Protein misfolding and amyloid nucleation through liquid–liquid phase separation. *Chem. Soc. Rev.* **53**, 4976–5013 (2024).

100. Ray, S. *et al.* α-Synuclein aggregation nucleates through liquid-liquid phase separation. *Nat Chem* **12**, 705–716 (2020).

101. Patel, A. *et al.* A Liquid-to-Solid Phase Transition of the ALS Protein FUS Accelerated by Disease Mutation. *Cell* **162**, 1066–1077 (2015).

102. Röntgen, A. *et al.* Aggregation of α-synuclein splice isoforms through a phase separation pathway. *Sci Adv* **11**, eadq5396 (2025).

103. Elbaum-Garfinkle, S. Matter over mind: Liquid phase separation and neurodegeneration. *J Biol Chem* **294**, 7160–7168 (2019).

104. Sneideris, T. *et al.* Targeting nucleic acid phase transitions as a mechanism of action for antimicrobial peptides. *Nat Commun* **14**, 7170 (2023).

105. Mugunthan, S. *et al.* RNA is a key component of extracellular DNA networks in Pseudomonas aeruginosa biofilms. *Nat Commun* **14**, 7772 (2023).

106. Chiba, A. *et al.* Staphylococcus aureus utilizes environmental RNA as a building material in specific polysaccharide-dependent biofilms. *NPJ Biofilms Microbiomes* **8**, 17 (2022).

107. Preissner, K. T. & Fischer, S. Functions and cellular signaling by ribosomal extracellular RNA (rexRNA): Facts and hypotheses on a non-typical DAMP. *Biochim Biophys Acta Mol Cell Res* **1870**, 119408 (2023).

108. Preissner, K. T., Fischer, S. & Deindl, E. Extracellular RNA as a Versatile DAMP and Alarm Signal That Influences Leukocyte Recruitment in Inflammation and Infection. *Front Cell Dev Biol* **8**, 619221 (2020).

Supplementary Information

RNA Selectively Modulates Activity of Virulent Amyloid PSMα3 and Host Defense LL-37 via Phase Separation and Aggregation Dynamics

Rayan *et al.*

The supplementary information contains:

Figures S1-S15

Movies S1-S2

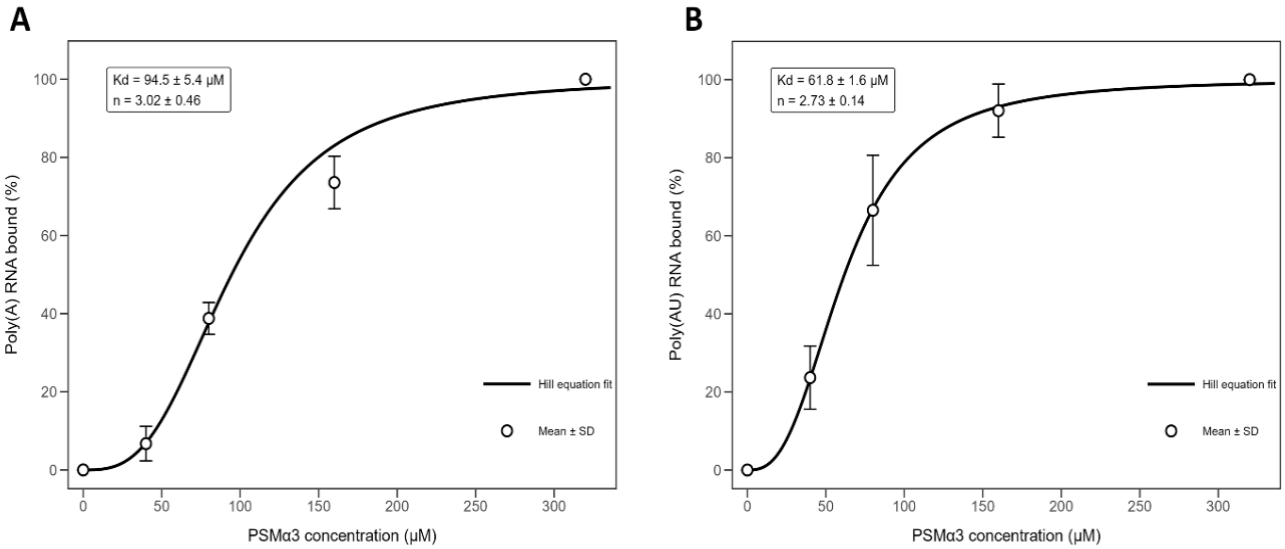

Figure S1. Concentration-dependent binding of PSMα3 to Poly (AU) and Poly (A) RNA. Percent RNA bound was quantified as a function of PSMα3 concentration for Poly AU) **(A)** and Poly(A) **(B)** calculated from the EMSA gels shown in Figure 1. Data points represent mean ± SD. Solid lines indicate fits to a Hill binding model with fixed asymptotes (0–100%). The apparent dissociation constant (Kd) corresponds to the protein concentration yielding 50% RNA binding, fitted Kd and Hill coefficient (n) values ± SE are shown.

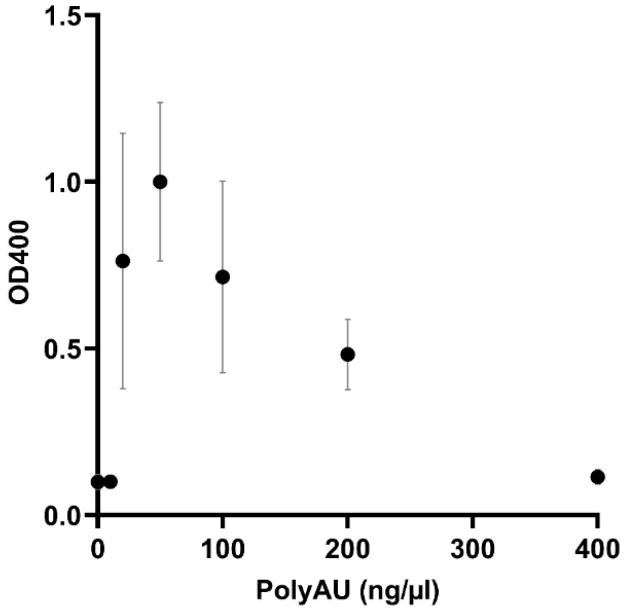

Figure S2. Turbidity measurements of PSMα3 with increasing Poly (AU) RNA concentrations. PSMα3 concentration was maintained at 100 µM, and Poly (AU) RNA concentrations varied across 0, 10, 20, 50, 100, 200, and 400 ng/µL. Data points represent the average optical density at 400 nm (OD400) recorded within the first 30 minutes post-resuspension, with each condition tested in triplicate. Error bars indicate the standard error of the mean.

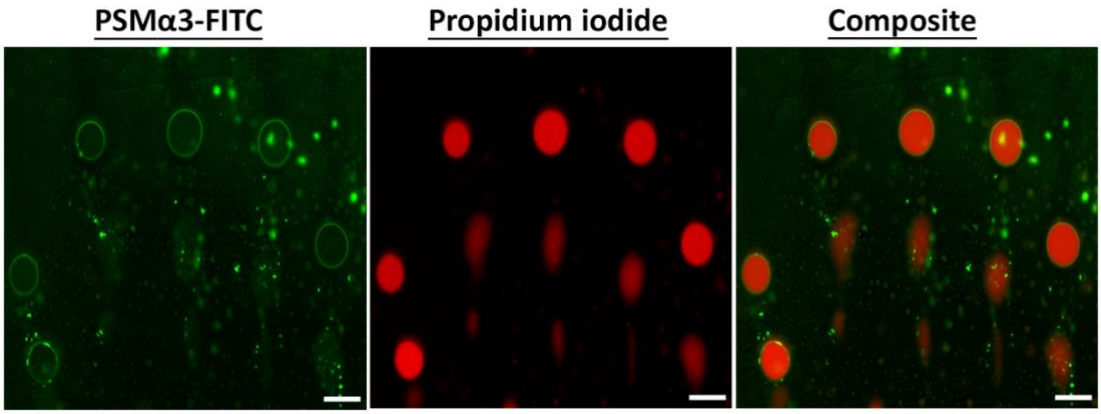

Figure S3. Encapsulation of Poly (AU) RNA within PSMα3-FITC droplets. 20% FITC-PSMα3 (green) and 80% unlabelled 100 μM PSMα3 were mixed with 50 ng/μL Poly (AU) RNA labelled with propidium iodide (PI). The left panel shows the FITC green channel, the middle panel displays the PI red channel, and the right panel is a composite image showing the overlap of PSMα3-FITC and Poly (AU) RNA-PI signals. Scale bars represent 20 μm.

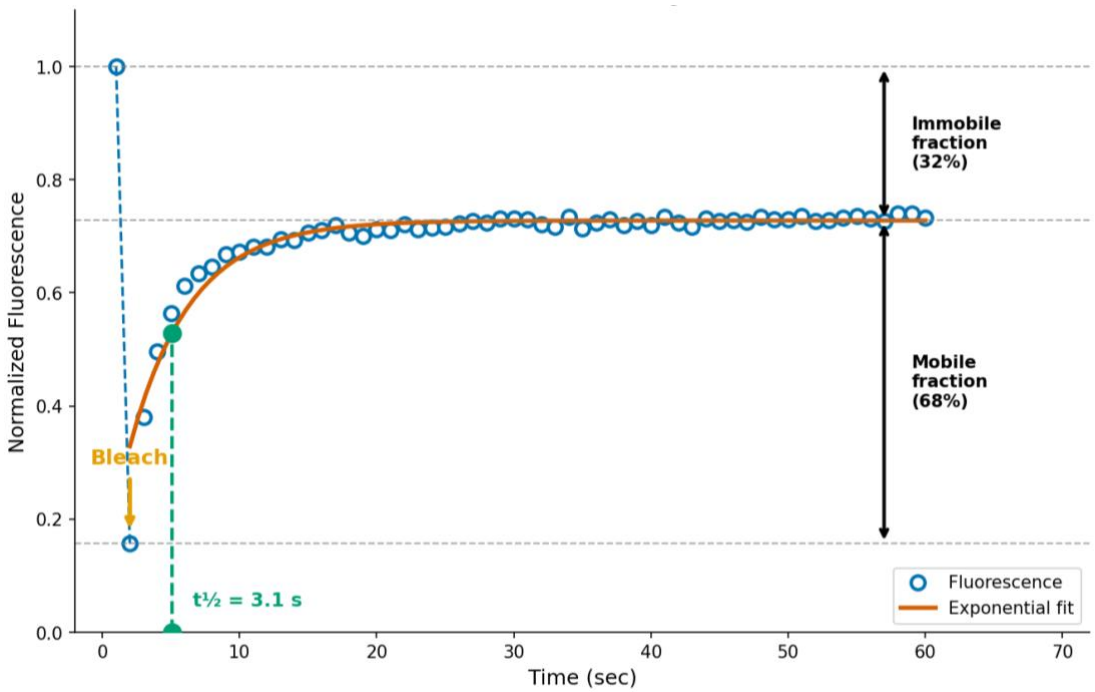

Figure S4. FRAP analysis of PSMα3 – Poly (AU) RNA condensate dynamics. Normalized fluorescence recovery after photobleaching (FRAP) measured within condensates formed by 20% FITC-PSMα3 (green) and 80% unlabelled 100 μM PSMα3 in the presence of 50 ng/μL Poly (AU) RNA, corresponding to the experiment shown in Figure 2. Blue circles represent measured fluorescence intensity normalized to pre-bleach levels, and the red curve indicates a single-exponential fit to the recovery phase. The bleach event is marked by the orange arrow. Recovery reaches a plateau corresponding to a mobile fraction of 68% and an immobile fraction of 32%. The green marker and dashed line denote the half-time of recovery (t½ = 3.1 s). Horizontal dashed lines indicate pre-bleach intensity (top), plateau recovery level (middle), and immediate post-bleach intensity (bottom).

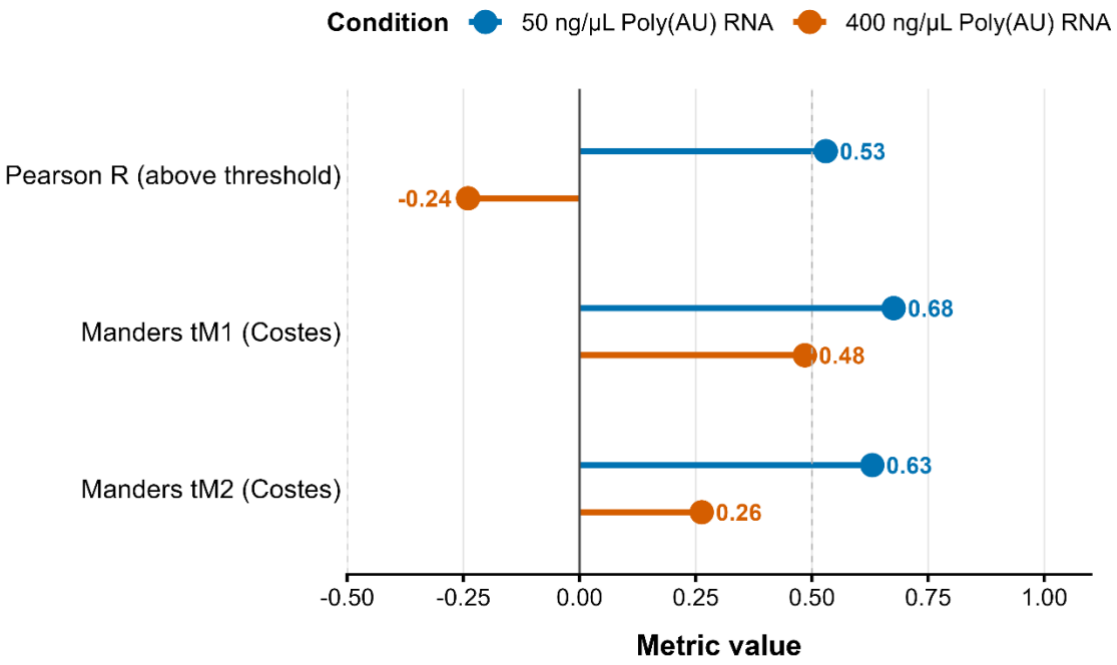

Figure S5. Colocalization analysis of PSMα3 and Poly (AU) RNA at different RNA concentrations. Quantitative comparison of colocalization metrics for 100 µM PSMα3 (20% FITC-PSMα3 and 80% unlabelled) and Poly(AU) RNA at 50 ng/µL (blue) and 400 ng/µL (orange), corresponding to the experiment shown in Figure 2. Pearson's correlation coefficient was calculated using above-threshold pixels only, with thresholds determined automatically by the Costes method. Additional metrics include Spearman's rank correlation coefficient (ρ), Li's intensity correlation quotient (ICQ), and Manders' colocalization coefficients (tM1 and tM2) calculated using Costes automatic thresholding. Numeric values for each metric are indicated on the plot. The dashed vertical line at 0.5 marks a commonly used reference value for strong colocalization.

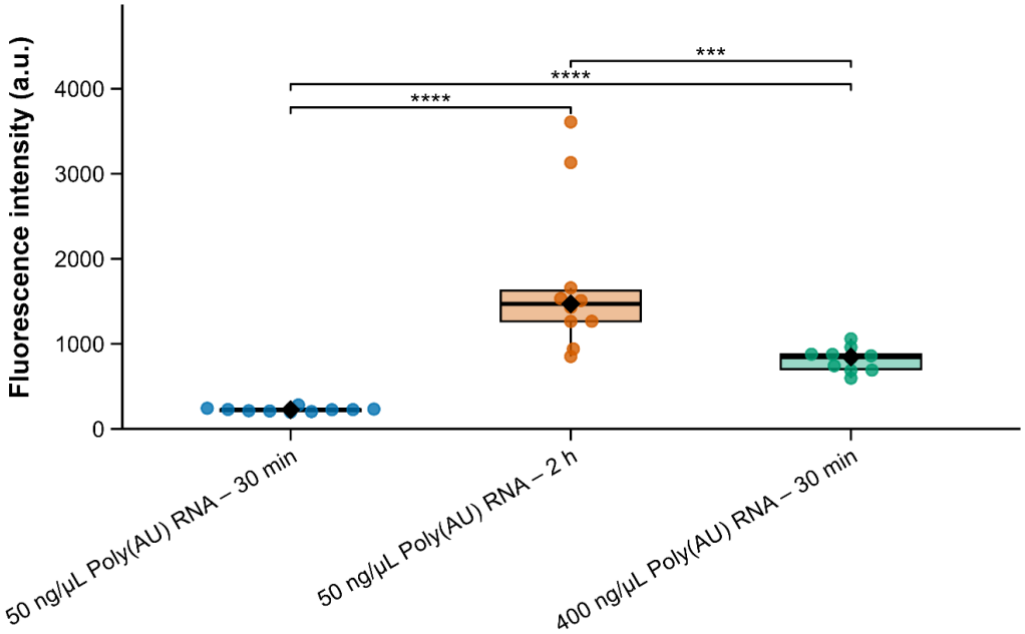

Figure S6. PSMα3 amyloid formation is enhanced by Poly (AU) RNA in a time- and concentration-dependent manner. The graphs show the calculated AmyTracker (AT630) fluorescence intensity of 100 µM PSMα3 incubated with Poly (AU) RNA under the indicated conditions, corresponding to the experiment shown in Figure 3. Boxplots show the interquartile range with the centre line indicating the median; black diamonds denote the mean. Individual points represent independent measurements. Statistical significance was assessed using a Kruskal–Wallis test followed by Dunn's post hoc test with Bonferroni correction. *$p < 0.05$, **$p < 0.01$, ***$p < 0.001$, ****$p < 0.0001$.

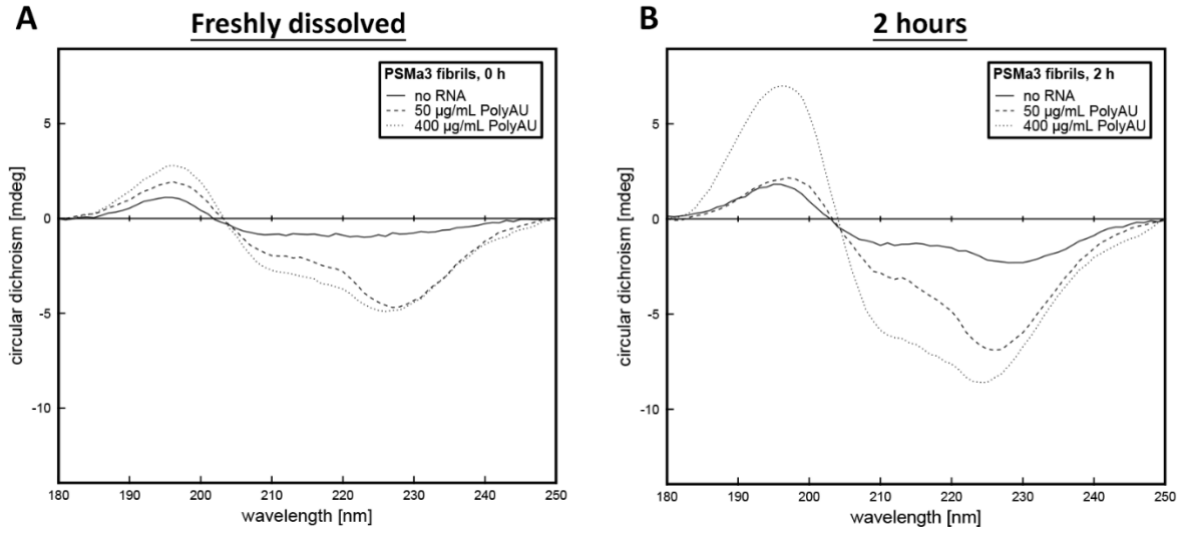

Figure S7. RNA stabilizes an α-helical conformation of PSMα3 over time. Solid-state circular dichroism (ssCD) spectra of 100 µM PSMα3 incubated alone or with poly (AU) RNA at concentrations of 50 ng/µL and 400 ng/µL. Spectra were collected immediately after preparation (**A**), and after 2 hours of incubation (**B**). Measurements were recorded in the far-UV range (180–250 nm) to assess changes in secondary structure under the indicated conditions.

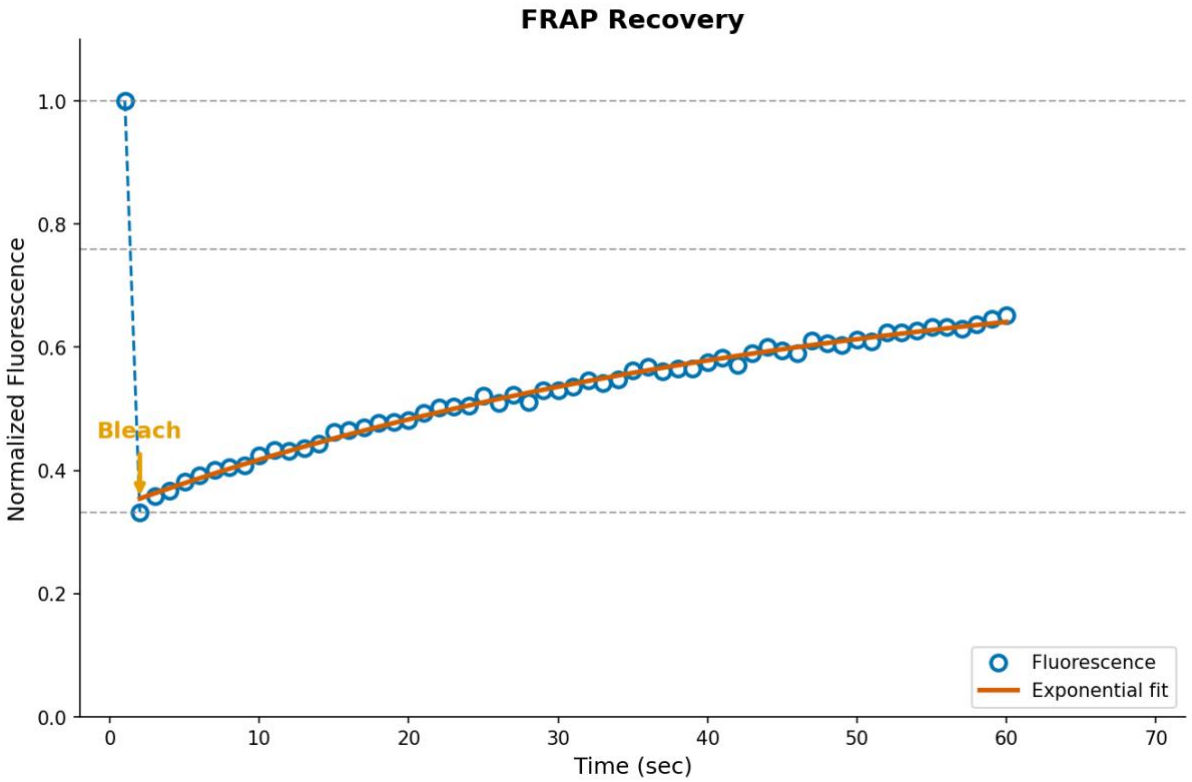

Figure S8. FRAP analysis of PSMα3 dynamics within the nucleolus of HeLa cells. Normalized FRAP of 20% FITC-PSMα3 and 80% unlabelled 20 μM PSMα3 measured within the nucleolus of HeLa cells, corresponding to the experiment shown in Figure 5. Blue circles represent fluorescence intensity values normalized to the pre-bleach signal, and the orange line shows a single-exponential fit to the recovery kinetics. The photobleaching event is indicated by the orange arrow. Over the 60 s acquisition window, fluorescence recovery reached ~64%, corresponding to a mobile fraction of ~64% and an immobile fraction of ~36%. The recovery did not reach a clear plateau within the measured time frame, indicating the presence of a slowly exchanging or partially immobilized PSMα3 population within the nucleolus.

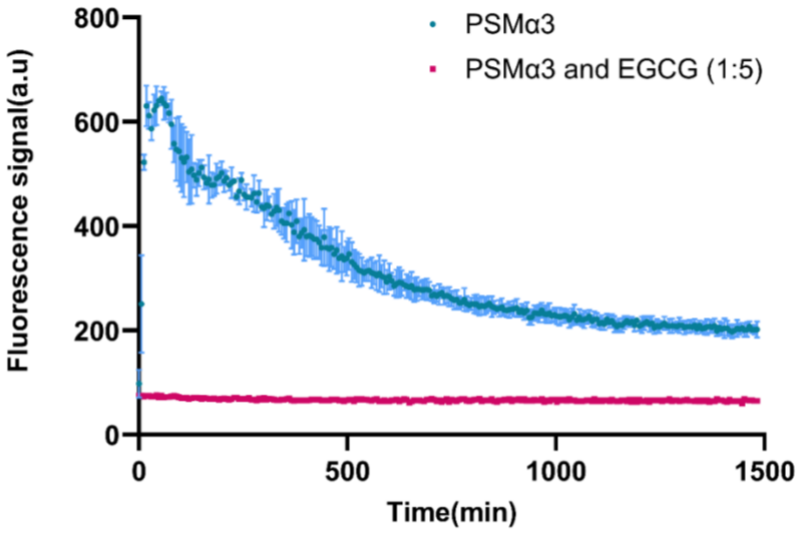

Figure S9. EGCG inhibits PSMα3 Fibrillation. Fibrillation kinetics of 100 μM freshly dissolved PSMα3, monitored by Thioflavin-T (ThT) fluorescence. The data compares PSMα3 fibrillation in the absence (blue curve) and presence (red curve) of EGCG. The graph displays the mean fluorescence intensities from triplicate ThT measurements, with error bars representing the standard error of the mean.

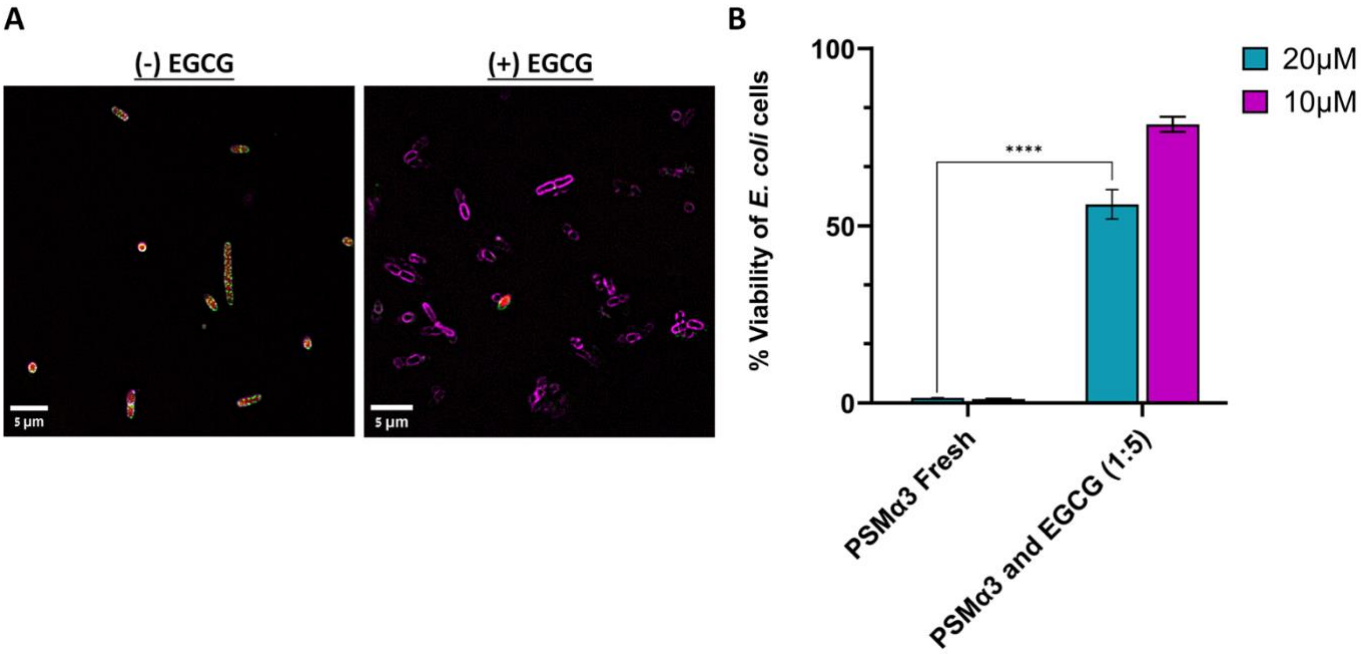

Figure S10. EGCG reduces the antimicrobial activity of PSMα3 against *E. coli*. (A) Super-resolution light microscopy images of *E. coli* treated with 20 µM of 20% FITC-PSMα3 (green) and 80% unlabelled PSMα3 in the absence (left) and presence (right) of EGCG at a 1:5 molar ratio. Scale bars: 5 µm. **(B)** Antimicrobial activity of PSMα3 against *E. coli*, evaluated using the PrestoBlue cell viability assay, with and without EGCG (1:5 molar ratio). The experiments were performed in at least three replicates and repeated across three independent days to ensure result reliability. Cytotoxicity and bacterial cell viability percentages were calculated as the mean of all replicates, with error bars representing the standard error of the mean (SEM). Statistical significance was determined using one-way ANOVA for normally distributed data in GraphPad Prism (version 11). Significance levels are indicated as follows: *$p<0.05$, **$p<0.01$, ***$p<0.001$, ****$p<0.0001$.

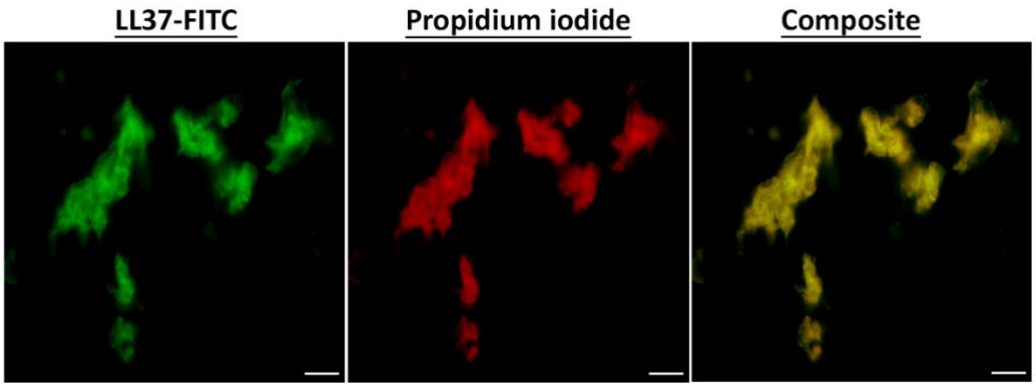

Figure S11. LL-37 undergoes aggregation with Poly (AU) RNA. Light microscopy images showing 20% FITC-labelled (green) and 80% unlabelled 100 μM LL-37 (with no thermal stress) forming aggregates in the presence of 100 ng/μL Poly (AU) RNA, stained with PI (red). The composite image (right) highlights the colocalization of LL-37 and RNA (yellow), indicating RNA-induced aggregation. Scale bars: 20 μm.

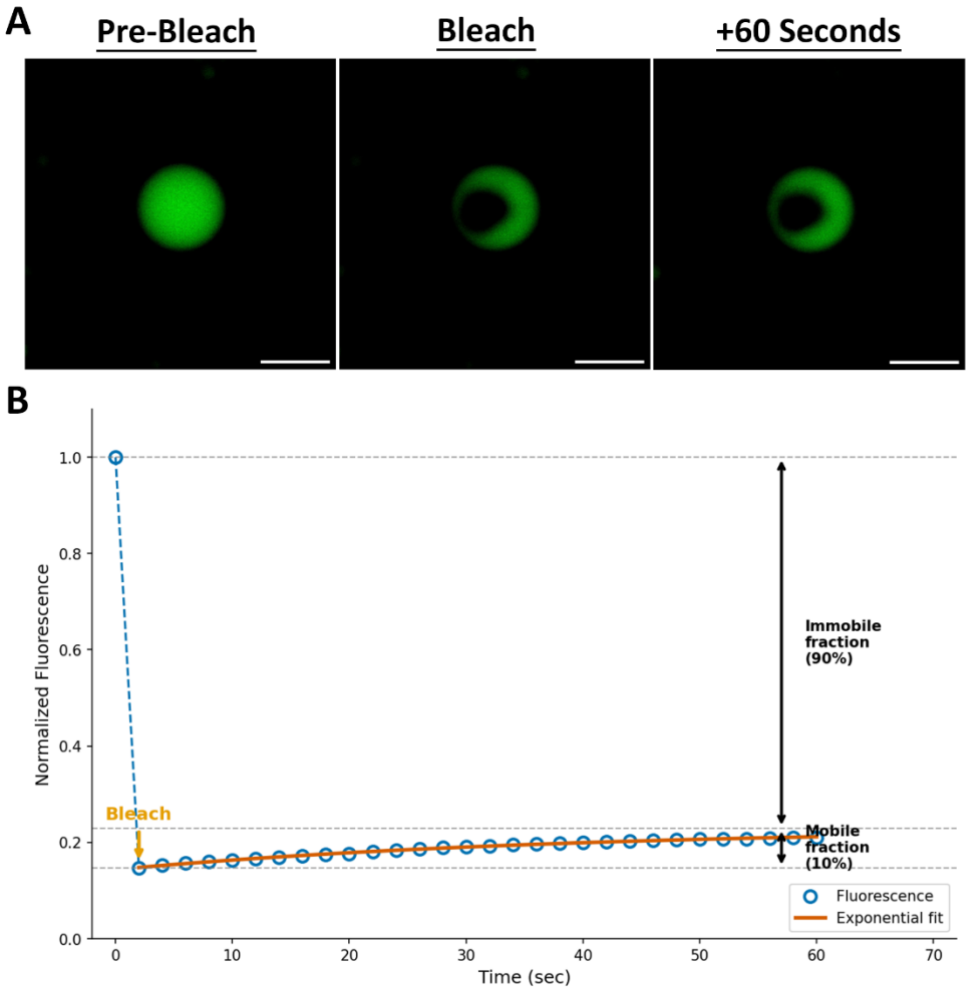

Figure S12. FRAP analysis of LL-37 – Poly (AU) RNA assemblies following heat shock. (A) Representative fluorescence images of 20% FITC-labelled (green) and 80% unlabelled 100 μM LL-37 assemblies formed in the presence of 100 ng/μL Poly(AU) RNA in UB7 buffer, shown before photobleaching (Pre-Bleach), immediately after photobleaching (Bleach), and 60 s after bleaching (+60 Seconds). **(B)** Normalized FRAP corresponding to the bleached region shown in (A). Blue circles represent fluorescence intensity normalized to pre-bleach levels, and the orange curve shows a single-exponential fit to the recovery data. The bleach event is indicated by the orange arrow. Recovery reaches a low plateau corresponding to a mobile fraction of 10% and an immobile fraction of 90%. Horizontal dashed lines denote pre-bleach intensity (top), plateau recovery level (middle), and immediate post-bleach intensity (bottom).

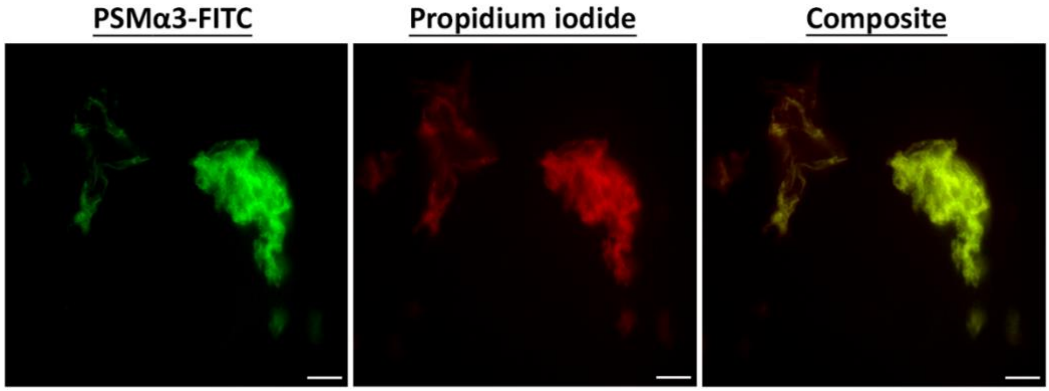

Figure S13. PSMα3 aggregates with Poly (AU) RNA after heat shock at physiological pH. Light microscopy images showing 20% FITC-PSMα3 (green) and 80% unlabelled 100 μM PSMα3 forming aggregates with 50 ng/μL Poly (AU) RNA, stained with PI (red), after heat shock at 60°C for 15 minutes in 50 mM HEPES, 150 mM NaCl, at physiological pH (7.4). The composite image (right) highlights the colocalization of PSMα3 and RNA (yellow), indicating RNA-induced aggregation under heat stress. Scale bars: 20 μm.

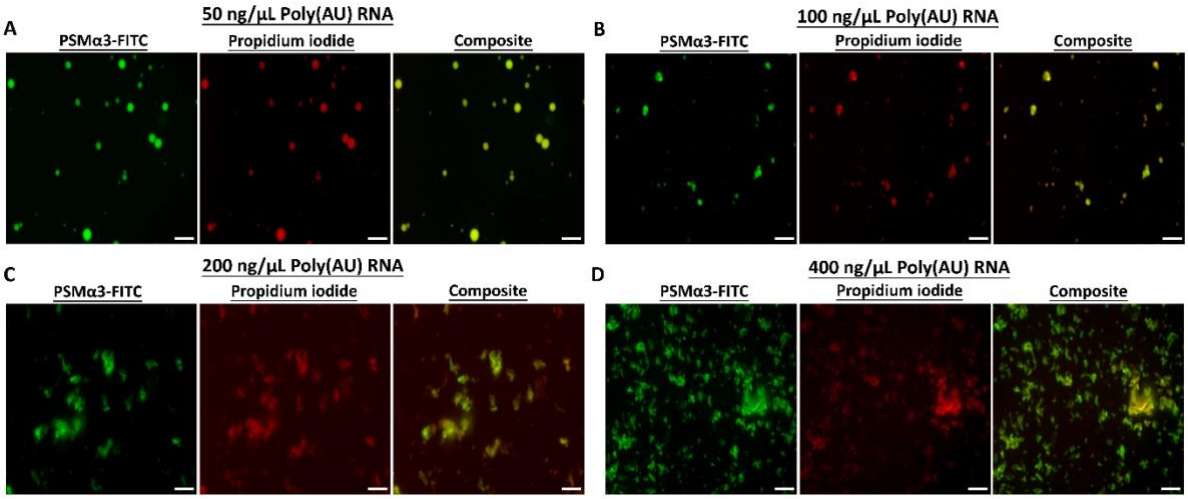

Figure S14. Effect of RNA concentration on PSMα3 phase separation and aggregation at pH 4 after heat shock. Fluorescence microscopy images showing the effects on 20% FITC-PSMα3 (green) and 80% unlabelled 100 µM PSMα3 in the presence of increasing concentrations of Poly (AU) RNA (labelled with PI, red) following heat shock at 65°C for 15 minutes at pH 4. at 50 ng/µL (**A**), 100 ng/µL (**B**), 200 ng/µL (**C**) and 400 ng/µL (**D**). At a low RNA concentration of 50 ng/µL (**A**), clear phase separation of PSMα3 was observed, as evidenced by the presence of well-defined, spherical droplets. As the RNA concentration increased to 100 ng/µL, the droplets began to lose their spherical structure and showed more morphological irregularities (**B**). At RNA concentrations of 200 ng/µL and 400 ng/µL, a distinct transition to aggregation with irregular, amorphous clusters were observed (**C** and **D**, respectively). The composite images revealed an overlap between the PSMα3 and RNA, indicating co-localization during both phase separation and amorphous cluster formation. Scale bars in all images represent 20 µm.

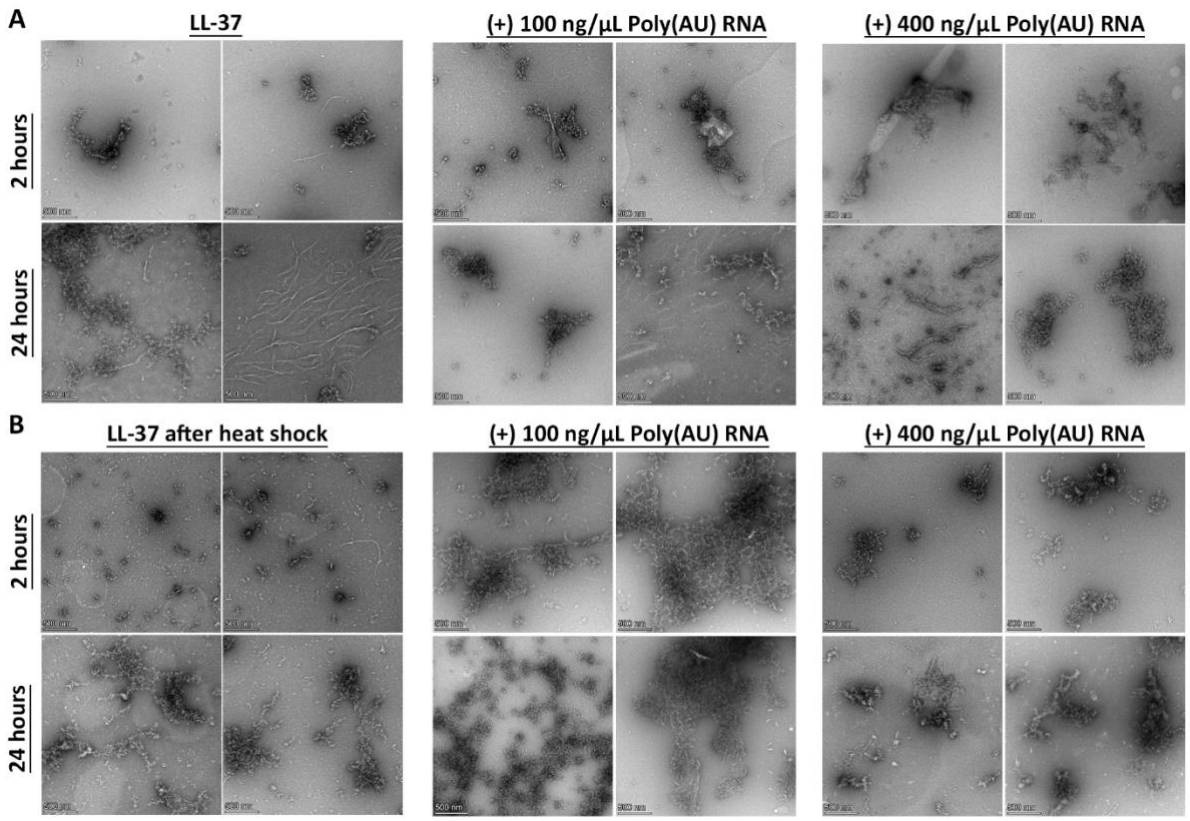

Figure S15. Poly (AU) RNA Modulates LL-37 Aggregation Dynamics Before and After Heat Shock. TEM micrographs of 100 µM LL-37 incubated alone or with 100 ng/µL or 400 ng/µL Poly (AU) RNA for 2 hours or 24 hours. **(A)** Samples imaged before heat shock at the indicated point. **(B)** Samples subjected to a 65°C heat shock for 15 minutes, followed by further incubation for 2 or 24 hours before imaging.

Movie S1. Live-cell imaging of PSMα3-induced membrane permeabilization in HeLa cells. HeLa cells were incubated with 20 μM of 20% FITC-PSMα3 (green) and 80% unlabelled PSMα3 and monitored by time-lapse fluorescence microscopy. Nuclei were stained with Hoechst (blue). PI (red) was present in the imaging medium to detect loss of plasma membrane integrity. Time is shown in minutes: seconds (mm:ss) from peptide addition. Scale bar, 10 μm.

Movie S2. Live-cell imaging of EGCG-modulated PSMα3 activity in HeLa cells. HeLa cells were incubated with 20 μM of 20% FITC-PSMα3 (green) and 80% unlabelled PSMα3 in the presence of EGCG at a fivefold molar excess relative to PSMα3 (PSMα3: EGCG = 1:5) and monitored by time-lapse fluorescence microscopy. Nuclei were stained with Hoechst (blue). PI (red) was present in the imaging medium to detect loss of plasma membrane integrity. Time is shown in minutes:seconds (mm:ss) from peptide addition. Scale bar, 10 μm.